

DESIGN AND SYNTHESIS OF A HIGH POTENTIAL RUTHENIUM (II)
TETRAAZATETRAPYRIDOPENTAPHENE COMPLEX
CAPABLE OF TWO-ELECTRON REDUCTION

by

NANCY RUTH G. DIAZ

Presented to the Faculty of the Graduate School of
The University of Texas at Arlington in Partial Fulfillment
of the Requirements
for the Degree of

MASTER OF SCIENCE IN CHEMISTRY

THE UNIVERSITY OF TEXAS AT ARLINGTON

August 2009

Copyright © by Nancy Ruth G. Diaz 2009

All Rights Reserved

ACKNOWLEDGEMENTS

I would like to express my deep gratitude to my research advisor, Dr. Frederick M. MacDonnell, for his patience, understanding, along with his guidance and encouragement throughout the course of my research. I also would like to thank Dr. H. V. Rasika Dias and Dr. Dennis S. Marynick, current and past members of my committee respectively, for their advice and inputs. Special thanks to Dr. Norma Tacconi, who in addition to being a member on my committee, was also responsible for obtaining the electrochemical data that are invaluable to our research. Her ebullient personality and her eagerness to help are well appreciated by many.

I would like to thank past and present members of Dr. MacDonnell's research group, David, Allen, Joseph, Amanda, Abishek, Fiona, Rungano, Arthi, Cale, Thamara, Kelly, and the postdocs Drs. Saha and Sezen for their valuable ideas and suggestions, their encouragement and their friendship. I also would like to acknowledge the help of Dr. Shreeyukta Singh whose suggestions were instrumental in obtaining the target compound, and Kenneth Abayan, who did the MO calculations that are very useful in explaining the empirical observations.

I am very grateful to the University of Texas at Arlington, the Dept. of Chemistry and Biochemistry in particular, for giving me the opportunity to pursue my graduate studies here. The department staff and the rest of the university staff are simply great and I would like to thank them all for their assistance.

I also would like to thank the National Science Foundation and the Welch Foundation for sponsoring the group's research on solar hydrogen production.

Special thanks to my family and friends, who have given words of encouragement and who helped me go through the tough times. Most especially to my parents and to my brother for their unwavering love and support, they are my pillar and my inspiration.

July 20, 2009

ABSTRACT

DESIGN AND SYNTHESIS OF A HIGH POTENTIAL RUTHENIUM (II) TETRAAZATETRAPYRIDOPENTAPHENE COMPLEX CAPABLE OF TWO-ELECTRON REDUCTION

Nancy Ruth G. Diaz, M.S.

The University of Texas at Arlington, 2009

Supervising Professor: Frederick M. MacDonnell

We report the synthesis of a complex, $[(\text{phen})_2\text{Ru}(\text{tatpp}_h)\text{Ru}(\text{phen})_2]^{4+}$ (\mathbf{P}_h^{4+}), which like its predecessor compound, $[(\text{phen})_2\text{Ru}(\text{tatpp}_c)\text{Ru}(\text{phen})_2]^{4+}$ (\mathbf{P}_c^{4+}), can undergo two sequential 1-electron photoreductions in MeCN in the presence of a sacrificial reductant. The initial complex, \mathbf{P}_h^{4+} , can be completely regenerated from the singly and doubly reduced forms by exposure to air, although the rate of regeneration for the second photoreduction is much slower than the first. Electrochemical studies have shown that this complex is not only capable of storing multiple reducing equivalents but these equivalents have stored potentials that are significantly higher than the complex \mathbf{P}_c^{4+} and are sufficient to reduce H^+ to H_2 . The first and second reduction potentials for \mathbf{P}_h^{4+} were determined to be at -0.53 and -0.96 V respectively, while the corresponding reduction potentials for \mathbf{P}_c^{4+} were found to be at -0.02 and -0.51 V, all reported vs. NHE. These results correlate very well with the MO calculations which predicted a \mathbf{P}_h^{4+} LUMO that is 0.56 eV higher in energy than the \mathbf{P}_c^{4+} LUMO. The internal coordination site, born out of the bridging ligand's bent structure, is also accessible to further structural modifications that may lead to improve photocatalytic properties for the complex.

TABLE OF CONTENTS

ACKNOWLEDGEMENTS	iii
ABSTRACT	iv
LIST OF ILLUSTRATIONS.....	vii
LIST OF TABLES	ix
CHAPTER	Page
1. INTRODUCTION.....	1
1.1 Background	1
1.2 Natural Photosynthesis	2
1.3 Artificial Photosynthesis	4
1.4 Photoinduced Energy and Electron Transfer	8
1.5 Properties Of $[\text{Ru}(\text{bpy})_3]^{2+}$	9
1.6 Multi-Electron Photocatalysts	12
1.7 Scope of Thesis	13
2. SYNTHESIS AND CHARACTERIZATION OF $[(\text{phen})_2\text{Ru}(\text{tatpp}_h)\text{Ru}(\text{phen})_2]^{4+}$	15
2.1 Introduction.....	15
2.2 Experimental	16
2.2.1 Materials and Measurements.....	16
2.2.2 Synthesis.....	17
2.3 Results and Discussion.....	18
2.3.1 Synthesis.....	18
2.3.2 Structural Characterization.....	21
2.3.3 Electronic Spectra	25
2.3.4 Electrochemistry.....	30

3. PHOTOCHEMICAL AND CHEMICAL SPECIATION OF $[(\text{phen})_2\text{Ru}(\text{tatpp}_h)\text{Ru}(\text{phen})_2]^{4+}$	36
3.1 Introduction.....	36
3.2 Experimental	36
3.3 Results and Discussion.....	37
3.3.1 Photoreduction of $[(\text{phen})_2\text{Ru}(\text{tatpp}_h)\text{Ru}(\text{phen})_2]^{4+}$ in MeCN.....	37
3.3.2 Chemical Reduction of $[(\text{phen})_2\text{Ru}(\text{tatpp}_h)\text{Ru}(\text{phen})_2]^{4+}$	40
3.3.3 Photoreduction of $[(\text{phen})_2\text{Ru}(\text{tatpp}_h)\text{Ru}(\text{phen})_2]^{4+}$ in water	44
3.4 Summary and Conclusion	45
APPENDIX	
A. ^1H NMR AND ESI-MS SPECTRA OF 10,11-diaminodppz.....	46
B. ^1H NMR, COSY AND ESI-MS SPECTRA OF tatpp_h	49
C. ^1H NMR AND COSY SPECTRA of P_h^{4+}	53
REFERENCES.....	56
BIOGRAPHICAL INFORMATION	62

LIST OF ILLUSTRATIONS

Figure	Page
1.1 Shares of the world total energy primary supply	1
1.2 Photosynthesis (light-dependent reactions)	4
1.3 Basic set-up for: (a) an artificial photosynthetic system. (b) photoelectrochemical synthesis cell	5
1.4 Dexter and Förster energy transfer mechanism	8
1.5 Molecular orbital diagram of $\text{Ru}(\text{bpy})_3^{2+}$ and the relevant electronic transitions	10
1.6 Schematic of the relation between ground and excited state potentials for $\text{Ru}(\text{bpy})_3^{2+}$	11
1.7 Reduction of water by a photocatalytic system based on $\text{Ru}(\text{bpy})_3^{2+}$	12
1.8 The multi-electron photocatalysts P_c^{4+} and Q^{4+}	13
1.9 The new complex $[(\text{phen})_2\text{Ru}(\text{tatpp}_h)\text{Ru}(\text{phen})_2]^{4+}$	14
2.1 Initial synthetic scheme for the synthesis of P_h^{4+}	19
2.2 Second synthetic scheme for the synthesis of P_h^{4+}	20
2.3 ^1H NMR spectrum of 10,11-diaminodppz	22
2.4 ^1H NMR spectrum of tatpp_h	23
2.5 ^1H NMR spectrum of P_h^{4+}	24
2.6 ESI-MS spectrum of the complex P_h^{4+}	25
2.7 UV-Vis spectra of (a) tatpp_h and tatpp_c and (b) P_h^{4+} and P_c^{4+}	26
2.8 MO energy diagram of tatpp_h , $[\text{Ru}(\text{phen})_3]^{2+}$, and P_h^{4+}	28
2.9 MO pictures for the relevant orbitals of tatpp_h and tatpp_c	29
2.10 Cyclic voltammograms for P_h^{4+}	31
2.11 Differential pulse voltammograms comparing the	

electroreduction of \mathbf{P}_h^{4+} and \mathbf{P}_c^{4+}	32
3.1 Evolution of the absorption spectra of \mathbf{P}_h^{4+} during photoirradiation in MeCN	38
3.2 Evolution of the absorption spectra of \mathbf{P}_h^{4+} on chemical reduction by cobaltocene in MeCN	41
3.3 MO energy diagram of \mathbf{P}_h^{4+} , \mathbf{P}_h^{3+} , and \mathbf{P}_h^{2+}	42
3.4 Evolution of the absorption spectra of \mathbf{P}_h^{4+} during photoirradiation in water	43
3.5 MO diagram of \mathbf{P}_c^{4+} and \mathbf{P}_h^{4+} and their approximate LUMO energies	44
3.6 Structure of the planned complex, $[\mathbf{P}_h\text{PtCl}_2]^{4+}$	45

LIST OF TABLES

Table	Page
2.1 Reaction conditions for the synthesis of \mathbf{P}_h^{4+} , modified vs. original procedure.....	21
2.2 Redox potentials for the complexes \mathbf{P}_h^{4+} and \mathbf{P}_c^{4+}	34

CHAPTER 1
INTRODUCTION
1.1 Background

We cannot overemphasized the importance and the urgency to find alternative and renewable sources of energy, especially in the face of recent record spikes in fuel prices, worsening problem of global warming, and the increasing threat to global energy security.¹ Research in this area should not only be given priority but must be done with a sense of urgency, and indeed, there has been increased awareness of the importance of this effort. Having a clean and sustainable energy strategy has started to become part of the U.S. government's major policy decisions.² The green economy has been much talked about and has increasingly become an important component of the economy, and is very well posed to become the economy of the future.

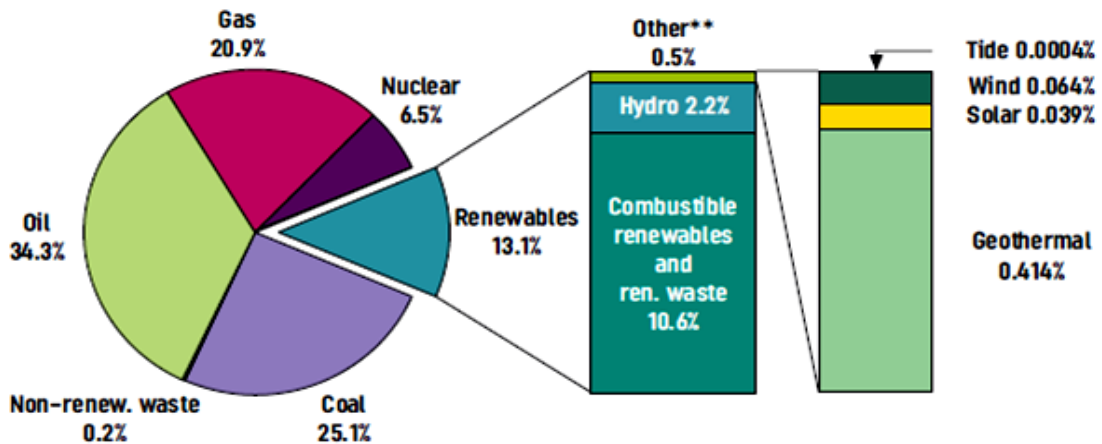


Figure 1.1 Shares of the world total energy primary supply.³

As seen in Figure 1.1, in 2004, only 13 percent of the world total energy primary supply comes from renewable energy and majority of this comes from traditional sources like hydropower, combustible renewables and renewable wastes, and geothermal.³ Solar energy

only contributed 0.04 % of the total, yet the sun provides a virtually unlimited supply of energy. Although the energy that can be collected from the sun is intermittent and varies according to location, on the average, each square meter of the earth's surface can collect the equivalent of 170 joules per second.⁴ If the sun's energy is collected for 2 days on approximately 10 percent of the earth's total land surface area it can theoretically supply the world's total annual energy needs of 450 EJ a year.

Current technologies for collecting and storing solar energy like solar thermal systems, photovoltaics, and solar power concentration systems are expensive and inefficient and have prevented solar energy from becoming a major energy source. Once these problems are overcome, we will have a clean and inexhaustible source of energy that is available to almost all regions of the world. Among current research initiatives on solar power technology, one that has gained recent interest is artificial photosynthesis. By mimicking some aspects of natural photosynthesis, it aims to convert the sun's energy into high-energy chemicals that can be stored for later use. A sunlight driven water-splitting reaction makes for a very attractive solution to the energy problem. Water and sunlight are both abundant and renewable, and one of the end products of this reaction is hydrogen. Hydrogen as a fuel is environmentally clean, giving back water as a combustion product, and is a very good energy carrier. Hydrogen when combined with oxygen releases a large amount of energy per unit mass.

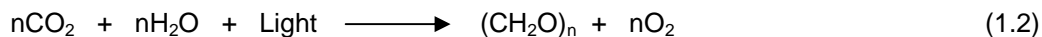


The chemical energy stored per kilogram of hydrogen is 142 MJ, which is at least three times more than petroleum based fuels.⁵ Given the right breakthroughs in research, this technology may well be the solution to our energy problem.

1.2 Natural Photosynthesis

Nature found a way to harness the almost inexhaustible source of energy provided by sunlight and convert it into high energy chemicals for organisms to use. This process is called photosynthesis and occurs in plants, some algae, and bacteria. The process involves several

steps and several intermediates, and for oxygenic photosynthesis the overall process can be summarized in the following chemical equation:



where $(\text{CH}_2\text{O})_n$ is a starch or a sugar with similar empirical formula to starch.⁶ Photosynthesis occurs in two stages, the light, and dark reactions. It is in the light reactions where the capture of light energy and the conversion into high energy molecules (ATP and NADPH) occur. These high energy molecules are subsequently used in the dark reaction step to fix CO_2 into carbohydrates. Of the two processes, the light reactions are more interesting to those involved in the photocatalytic splitting of water. Aside from being the light-to-chemical energy conversion step, it is where the water-splitting reaction occurs to provide oxygen and protons. In oxygenic photosynthetic organisms, the light reactions are carried out by photosystem I (PSI), photosystem II (PSII), the cytochrome b_6f complex, and the ATP synthase as shown in Figure 1.2. All these can be found in the thylakoid membranes. Each photosystem consists of light-harvesting antenna complexes, reaction centers and its associated electron transport proteins.⁷ The antenna complexes are made up of a large number of pigments like chlorophyll, which absorb light at 680 nm for PSII and 700 nm for PSI. When light is absorbed by the antenna complex at PSII it transfers this energy to a photoactive pigment (the reaction center chlorophyll), raising an electron to a higher energy level. This is subsequently quenched by electron transfer to a primary electron acceptor triggering a series of electron transfers called the Z-scheme. When the electron reaches PSI it is excited again to a higher potential by light absorption and this potential is then used to reduce NADP^+ to NADPH. Concomitant with the electron transfer process is the creation of a proton gradient that is used in the formation of ATP. To repeat the cycle, PSII has to be reduced back to its initial state so it can absorb light again. This electron comes from a catalytic center called the oxygen-evolving complex (OEC), a tetramanganese complex that goes through a series of oxidation states, S_0 , S_1 , S_2 , S_3 , S_4 , leading to the oxidation of water to O_2 and H^+ .⁶⁻⁹

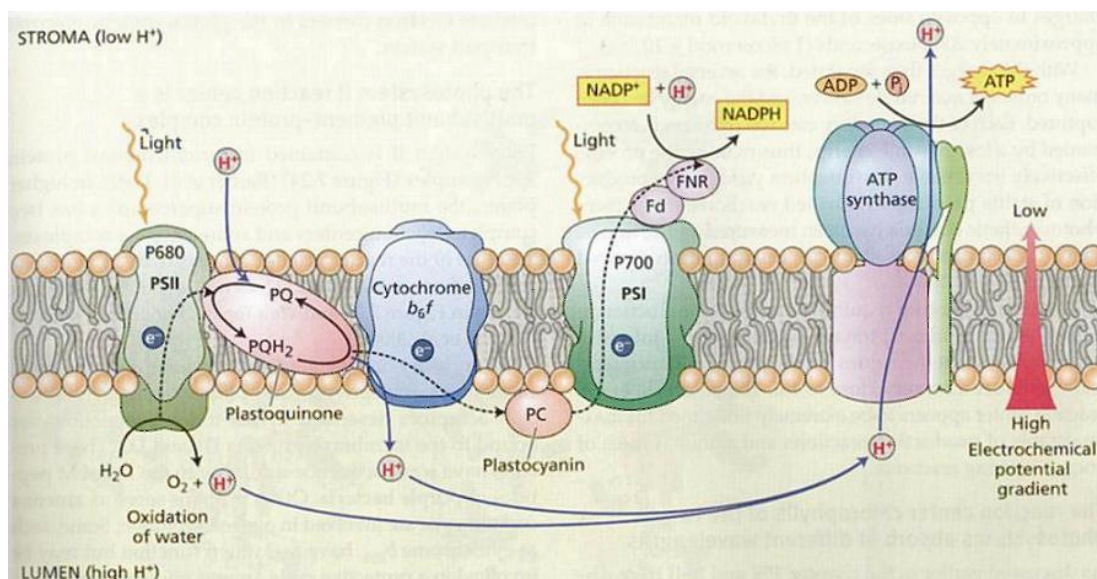


Figure 1.2 Photosynthesis (light-dependent reactions).⁷

1.3 Artificial Photosynthesis

Mimicking photosynthesis is a daunting task. Natural photosynthetic systems are inherently complex structures and the mechanisms involved are still not fully understood. However, significant advances in recent years in transition metal chemistry and in the elucidation of photosynthetic mechanisms have renewed interest in artificial photosynthesis.¹⁰ Building a commercially viable photosynthetic system may still be a long way off, but future success will definitely be built on past and current research initiatives.

Integrating the major photosynthetic components of light absorption, electron transfer and redox catalysis into a working assembly is not simple. It requires building a device that is robust, can efficiently absorb and transfer light energy, and has excellent catalytic activity. It must also have the right kinetics and energetics to drive the desired chemical reaction, namely proton reduction and water oxidation. Faced with these challenges, many researchers have approached the problem from a bottom-up perspective, where individual components, mimicking the different aspects of natural photosynthesis, are studied and built separately and later integrated into a single device.¹¹ There are myriad ways to organize the different

components into a working assembly. One way is to utilize polymer supports,¹² including proteins,¹³ to hold and organize the various components together. Another is to carry out the half-reactions at separate electrodes of a photoelectrochemical synthesis (PES) cell,¹⁴ Figure 1.3b. In a PES cell, the potential is provided by light where absorption and subsequent excited state electron transfer occur in a photoactive molecular device that link both electrodes. The photoactive material may be made up of a semiconductor,¹⁵⁻¹⁷ a transition metal complex or a combination of both.¹⁸ Still another method is to organize the various functional groups into a single supramolecular assembly held together by intramolecular or intermolecular attractive forces, Figure 1.3a.¹⁹⁻²⁵

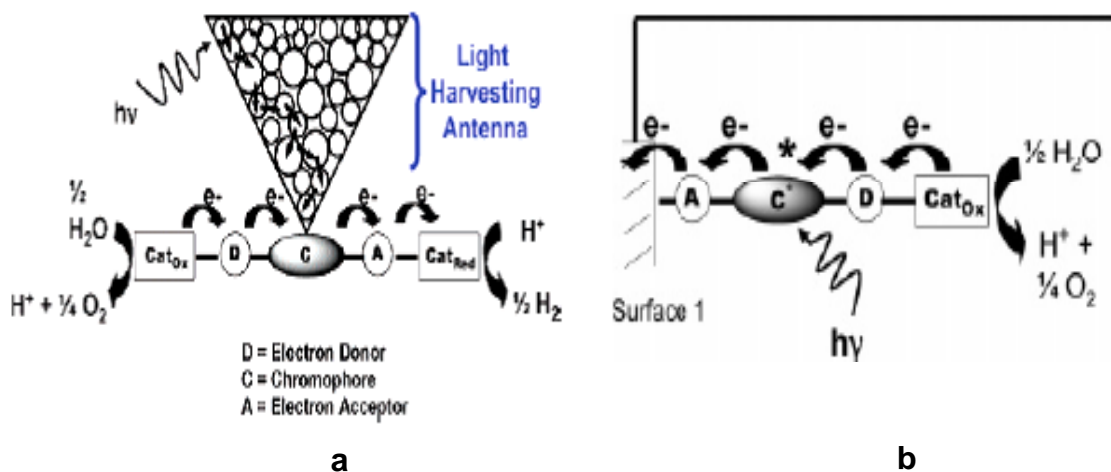


Figure 1.3 Basic set-up for (a) an artificial photosynthetic system (b) photoelectrochemical synthesis cell.¹⁴

Although the application of artificial photosynthesis is not limited to the splitting of water to produce H₂ and O₂, this reaction is generating the most interest and is the most relevant to current times. As varied as the approaches are to building a device for solar hydrogen production, there are basic guidelines or requirements to building a working and efficient device. These are:

- The system must be photochemically as well as electrochemically robust.
- Efficiently absorbs light in the visible region.
- The excited state lifetime is sufficiently long-lived for electron transfer to occur.

- The final charge-separated state has the right potentials to drive the water splitting reaction.

Central to any artificial photosynthetic system is the chromophore or the photosensitizer. This light-harvesting component determines how efficient sunlight is absorbed and whether absorption occurs at wavelengths that have sufficient energy to drive the desired photochemical reaction. The majority of sunlight falls in the range 400-750 nm. When absorbed, that translates to an excitation of between 3.10 and 1.65 eV for the photosensitizer.^{25, 26} With four successive absorptions needed to collect the four redox equivalents required to split water, this range of energies should be sufficient to drive the water-splitting reaction shown in Equation 1.5.



A system that has an oxidizing free energy $\leq -4.92 \text{ eV}$ ($4 \times -1.23 \text{ eV}$) or a reducing free energy $\leq -1.64 \text{ eV}$ ($2 \times -0.82 \text{ eV}$) should in principle be able to oxidize water to oxygen or reduce water to hydrogen at any pH respectively.^{27, 28}

However, the thermodynamics and kinetics of the whole process are not as straightforward as they may first appear. There are several variables that have to be considered, e.g. competing excited state deactivation processes and back electron transfer reactions. For the most part, the free-energy content of the final charge separated state will be smaller than the excited state. Therefore, efforts are being made to minimize the loss of energy during the series of electron transfers and obtain sufficient potential to drive the water-splitting reaction. Also, there have been efforts to use antenna complexes to maximize absorption in the solar spectrum and to funnel this energy to a single reaction center just like in natural photosynthesis.^{14, 29}

Water oxidation is not only energetically demanding but electronically as well. It requires a 4-electron oxidation and the first step in a series of one-electron oxidations involves a high-energy hydroxyl ($\cdot\text{OH}$) radical intermediate. Because of this energetic constraint, researchers have been looking at alternate mechanisms, and it has been suggested that a concerted two or four-electron oxidation of water would be more energetically favorable.^{28, 30} Meyer et al.^{25, 31} have reported photocatalytically producing O_2 using a ruthenium-oxo complex, and the photocatalyst was determined to undergo a concerted multi-electron oxidation of water.³² Bernhard et al.³³ also reported producing O_2 using another type of ruthenium-oxo complex, but the exact mechanism has yet to be determined.

Reduction of water, on the other hand, is more energetically and electronically favorable than the oxidation of water, but it does not mean that it is a facile reaction, it remains endogonic and would still require two electrons to complete the reduction. It is therefore advantageous for a hydrogen evolving system to also have the ability to undergo a concerted multi-electron reduction. MacDonnell's lab^{25, 34, 35} and Brewer's^{20, 36} group were able to synthesize compounds that are capable of storing multiple electrons, which is a significant step to building an efficient water reduction system

Although the ultimate goal is to build a complete water-splitting system, most of the efforts are focused on one half or the other of the water-splitting reaction. And for these half-reaction prototypes, sacrificial reductants, e. g., triethylamine (TEA),^{21, 34} or sacrificial oxidants, e.g., Ce(IV) salts,^{32, 33} are normally used to complete the redox process and prevent back-electron transfer reactions.^{37, 38}

Transition metal complexes easily lend themselves to applications in artificial photosynthesis because their photophysical and photochemical properties can be easily tuned through various ligand and metal combinations to match the requirements of the system.^{39, 40} Optical and redox properties of transition metal complexes are especially sensitive to changes

in the ligands and the metal core as these usually result in changes in the relative ordering of orbital energies.^{41, 42}

1.4 Photoinduced Energy and Electron Transfer

A knowledge of the underlying principles of photoinduced energy and electron transfer is fundamental to an understanding of the photosynthetic process. These are quenching mechanisms that may occur with the intrinsic radiative and non-radiative decay mechanisms for excited state deactivation. Quenching by energy transfer as shown in the following equation



is used in natural photosynthesis as a means for funneling energy from an antenna array of chromophores to the reaction center. An array of antenna complexes that can absorb sunlight at a much broader spectral range is attractive because it results in a more efficient collection of energy.¹⁴ Energy transfer may involve an electron exchange between the donor and acceptor (Dexter mechanism) or a dipole-dipole interaction (Förster mechanism), Figure 1.4. In the Dexter mechanism, energy transfer involves the simultaneous exchange of an electron from the HOMO of the acceptor to the HOMO of the donor and from the LUMO of the donor to the LUMO of the acceptor. For it to work there must be overlap of the wavefunctions of the donor and the acceptor, and so, is effective only at short distances. In the Förster mechanism or FRET (Förster resonance energy transfer), energy transfer occurs when the oscillating electric field of

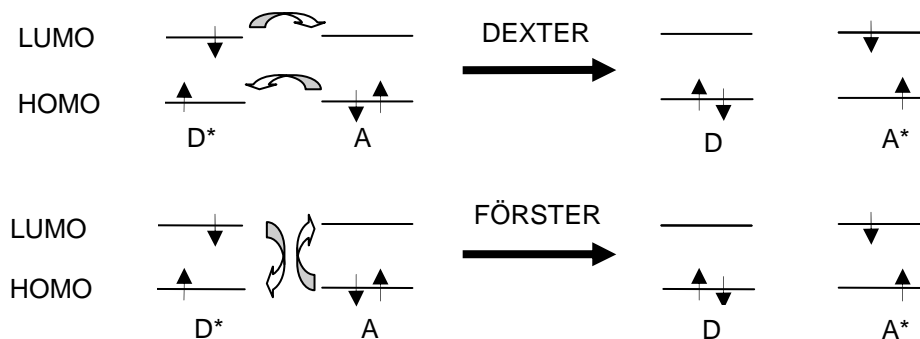


Figure 1.4 Dexter and Förster energy transfer mechanism.

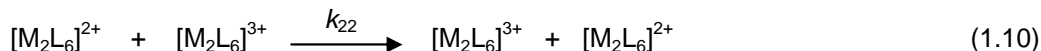
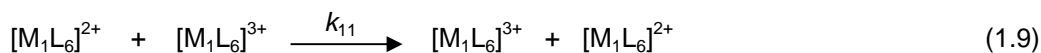
the donor is in resonance with the HOMO-LUMO gap of the acceptor. In other words, there must be spectral overlap between the emission and absorption spectra of the donor and acceptor respectively.⁴³ Compared with the Dexter mechanism, FRET is more effective at longer distances.^{44, 45}

Excited state quenching may also occur by electron transfer. The excited donor (D^*), because of its higher energy content, has a greater potential to donate or accept electrons than the corresponding ground-state as shown in the following reactions.³⁸

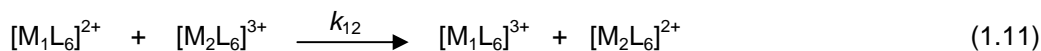


Photoinduced electron transfer is the mechanism by which photosynthesis converts light to chemical energy where the potential gradient resulting from the photoinduced charge separation is used to drive an electrochemical reaction.

Early theoretical work on electron transfer was primarily done by Marcus from observations of self-exchange reactions.



This was later extended to cross-reactions



and to other types of electron transfer reactions. The Marcus theory has been widely applied to organic compounds, organometallic complexes as well as biological systems. Approximations made from this relation generally agree with experimental data and deviations indicate a distinctive property in the outer-sphere mechanism or another mechanism is in effect.⁴⁶⁻⁴⁹

1.5 Properties Of $[Ru(bpy)_3]^{2+}$

One of the most widely investigated classes of chromophores is based on metal polypyridyl complexes which are known for their excellent photophysical and photochemical

properties. This class of compounds is generally robust and the ground and excited states as well as the different oxidation states are relatively stable.^{38, 41, 50, 51}

Since Gafney and Adamson⁵² first reported on the photoinduced electron transfer reaction of $[\text{Ru}(\text{bpy})_3]^{2+}$ (bpy = 2,2'-bipyridine), and following a suggestion by Sutin and Creutz⁵⁰ that the reaction can be used to split water, the ruthenium polypyridyl complexes have since generated a lot of interest and had been extensively studied. A discussion of the properties of $[\text{Ru}(\text{bpy})_3]^{2+}$, which are well known and well understood, can give us better insight into the properties of other related compounds.

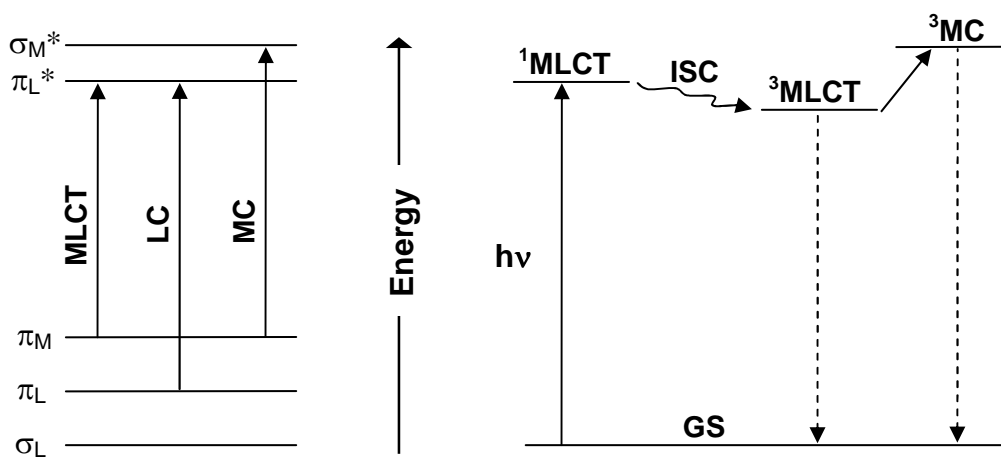


Figure 1.5 Molecular orbital diagram of $[\text{Ru}(\text{bpy})_3]^{2+}$ and the relevant electronic transitions.

The complex $[\text{Ru}(\text{bpy})_3]^{2+}$ has a pseudo-octahedral geometry with a D_3 symmetry which is reflected in its electronic structure.²⁷ Its UV-Visible spectrum is dominated by three types of transitions, the metal-to-ligand charge transfer (MLCT), metal centered (MC), and ligand centered (LC) transitions as shown in Figure 1.5. The $^1\text{MLCT}$ absorption at around 450 nm is a $d\pi - \pi^*$ transition that is predominantly singlet in character. This transition is followed by an intersystem crossing to the lowest excited $^3\text{MLCT}$ state that is basically triplet in character. The process is fast ($\tau < 1$ ps) and efficient ($\phi \sim 1$), a result of a considerable amount of spin-orbit coupling in the ruthenium metal core.^{14, 27} Emission subsequently occurs from the $^3\text{MLCT}$

excited state at around 600 nm in aqueous solutions. It has a relatively long lifetime of around 0.6 μs in water at 25°C, making it accessible to further electron transfer reactions.³⁸ Because of light absorption, the driving force for electron transfer reaction is enhanced in the excited state by 2.1 eV, the excitation energy, resulting in an excited state reduction and oxidation potential of 0.8 V and -0.8 V vs. SCE respectively, Figure 1.6. This extra energy may be used to drive an endoergic reaction that would not occur under normal conditions in the absence of light.¹⁴ For most ruthenium polypyridyl complexes the promoted electron is believed to be localized on a single ligand, and for heteroleptic complexes, this ligand will most likely be the one with the most positive reduction potential.³⁸

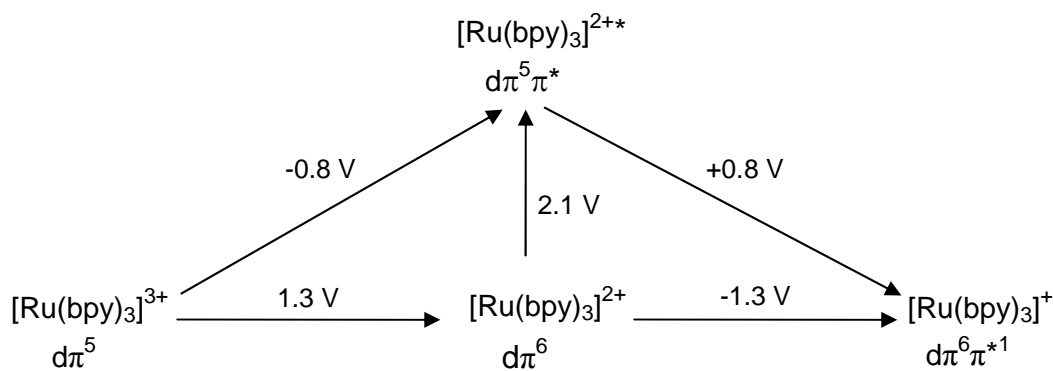


Figure 1.6 Schematic of the relation between ground and excited state potentials for $\text{Ru}(\text{bpy})_3^{2+}$ (vs. SCE in CH_3CN at 25°C).

The ^3MC excited state of $[\text{Ru}(\text{bpy})_3]^{2+}$ is short-lived and is thermally accessible from the $^3\text{MLCT}$ state shortening the excited state lifetimes of $[\text{Ru}(\text{bpy})_3]^{2+}$ at higher temperatures. Population of the ^3MC state may also lead to ligand loss. This is a result of the promotion of an electron from a non-bonding $d\pi$ orbital to an anti-bonding $d\sigma^*$ orbital which weakens the metal-ligand σ bond.³⁸ Because of these undesirable effects, different ways to raise ^3MC relative to $^3\text{MLCT}$ were being investigated and one approach was to use strong-field ligands to raise the energy of $d\sigma^*$ relative to the other orbitals.⁴²

An early polypyridyl based system for solar hydrogen production uses $[\text{Ru}(\text{bpy})_3]^{2+}$ as photosensitizer, MV^{2+} as an electron relay, a colloidal dispersion of platinum as co-catalyst, and

EDTA as electron donor, Figure 1.7.³⁷ Upon light excitation, $[\text{Ru}(\text{bpy})_3]^{2+}$ is oxidatively quenched by MV^{2+} to yield a $\bullet\text{MV}^+$ radical with $E^\circ = -0.44 \text{ V vs. NHE}$. At this potential, in the presence of Pt, it is capable of reducing water to H_2 , but because the rate of formation of the $\bullet\text{MV}^+$ radical and the reduction potential for H_2 formation are pH-dependent it works only at a certain pH range and the yield starts decreasing rapidly at low pH and at $\text{pH} > 6$.³⁸ Although far from perfect, this system has become the prototype to more complex systems including multi-component supramolecules.

1.6 Multi-Electron Photocatalysts

As discussed earlier in this chapter, the ability of a photocatalyst to store multiple reducing and oxidizing equivalents is highly desirable, if not necessary.²⁵ Oxidation or reduction of water can, in principle, occur through a 1-electron mechanistic pathway, but the energy requirements is so high, especially in the oxidation of water, that the reaction becomes highly inefficient to ever be economically feasible for energy production.

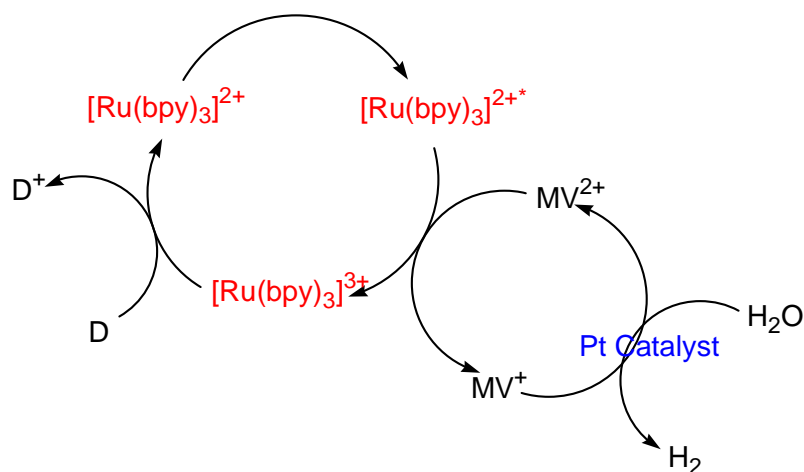


Figure 1.7 Reduction of water by a photocatalytic system based on $[\text{Ru}(\text{bpy})_3]^{2+}$.

The first to report a multi-electron photoreduction of a complex was Brewer et al.²⁴ where on photoexcitation, the trinuclear complex $[(\text{bpy})_2\text{Ru}(\text{BL})\text{Ir}(\text{BL})\text{Ru}(\text{bpy})_2]^{5+}$, can store one electron each on the π systems of two bridging ligands (BL). More recently, the same group reported producing H_2 using a rhodium-centered trinuclear complex,

$[(bpy)_2Ru(dpp)RhCl_2(dpp)Ru(bpy)_2]^{5+}$. This complex undergoes a 2-electron photoreduction of the central rhodium metal (Rh^{3+} to Rh^+) with a concomitant loss of the chloride ions, but preserving the supramolecular core. It has been suggested that the freed coordination sites can be used for further reactions with substrates.^{20, 36}

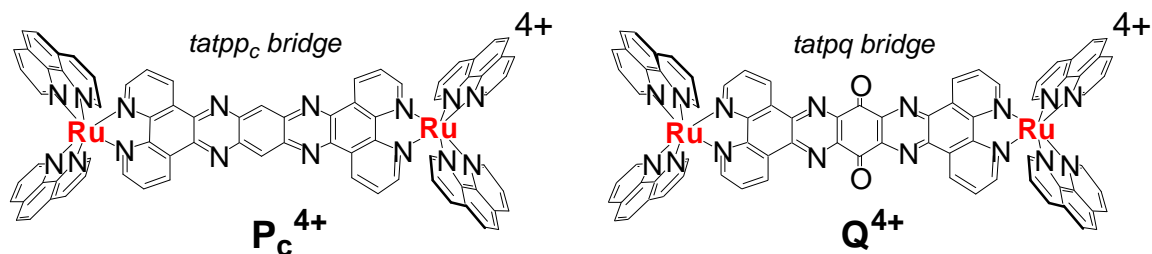


Figure 1.8 The multi-electron photocatalysts P_c^{4+} and Q^{4+} .

Our group was able to synthesize two dinuclear ruthenium complexes, $[(phen)_2Ru(tatpp_c)Ru(phen)_2]^{4+}$ (P_c^{4+}) and $[(phen)_2Ru(tatpq)Ru(phen)_2]^{4+}$ (Q^{4+}), Figure 1.8, that are capable of 2 and 4 electron reductions of the pyrazine and quinone portions of the bridging ligands respectively. At neutral to high pH in an aqueous medium, P_c^{4+} and Q^{4+} were shown to undergo a reversible, proton-coupled multi-electron reduction upon visible light irradiation. They also showed a high degree of photostability and were found to absorb strongly in the visible region.^{19, 34, 35} However, P_c^{4+} and Q^{4+} were not shown to produce significant quantities of hydrogen⁵³ and further investigations are currently being done in our group to improve the systems' capability to produce hydrogen.

1.7 Scope of Thesis

In this thesis, we will discuss the preparation as well as the structural, photophysical and photochemical characterizations of a new compound, $[(phen)_2Ru(tatpp_h)Ru(phen)_2]^{4+}$, Figure 1.9, where $tatpp_h$ is 9,12,21,22-tetraazatetrapyrido[3,2-a:2',3'-c:3''2''-m:2''' ,3'''-o]pentaphene and which we shall name P_h^{4+} from hereon. Although structurally similar to P_c^{4+} ,

the expectation is for P_h^{4+} to exhibit subtle but important differences in its photophysical and photochemical properties that will add value to P_h^{4+} as a potential photocatalyst.

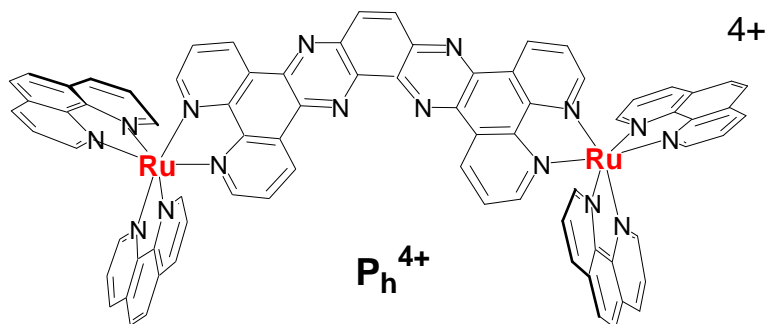


Figure 1.9 The new complex $[(phen)_2Ru(tatpph)Ru(phen)_2]^{4+}$.

In the second chapter, we will discuss the synthesis, the structural and the photophysical (optical and electrochemical) characterizations of the complex P_h^{4+} . While in the third chapter we will focus on the photochemistry of P_h^{4+} . A discussion of the chemical reduction experimental results will also be included in this chapter, which together with the MO calculations and the optical and electrochemical data will form the basis for explaining the photochemistry of P_h^{4+} .

CHAPTER 2

SYNTHESIS AND CHARACTERIZATION OF $[(\text{phen})_2\text{Ru}(\text{tatpp}_h)\text{Ru}(\text{phen})_2]^{4+}$

2.1 Introduction

With all the current problems associated with the use of fossil fuels and the recent heightened awareness of the importance of alternative energy research, our group's project on solar hydrogen production cannot be more timely and relevant.

\mathbf{P}_c^{4+} and \mathbf{Q}^{4+} are the two most widely studied compounds in our group and have been central to the group's research on solar hydrogen production for years. They are very stable compounds, absorb strongly in the visible region, and are shown to undergo a proton-coupled multi-electron photoreduction. However, their reduction potentials are not sufficiently negative to enable them to produce hydrogen efficiently, that is, the driving force to transfer the stored electrons is weak or absent. So our group continues to find ways to prepare potential photocatalysts that possess all the desirable features of \mathbf{P}_c^{4+} and \mathbf{Q}^{4+} and at the same time have the ability to reduce water more efficiently. One of the many efforts being pursued is the structural modification of the \mathbf{P}_c^{4+} and \mathbf{Q}^{4+} bridging ligands. Recently, we have prepared a new complex, \mathbf{P}_h^{4+} , that is structurally very similar to \mathbf{P}_c^{4+} except for its bent structure. Molecular orbital calculations using the DFT method have shown the LUMO of this complex is higher in energy than the LUMO of the complex \mathbf{P}_c^{4+} , i.e., it should have more stored energy or reducing potential than its linear analogue. And with the new complex retaining the two pyrazine units in its structure, it should also have the capability to store multiple electrons. The bent structure also resulted in a third coordination site which should easily lend the new complex to further functionalization. We have investigated the photophysical and photochemical properties of this new compound to determine whether theoretical predictions correspond with empirical observations and whether it can be a viable photocatalyst.

The complex P_h^{4+} was prepared based on existing literature procedures with slight modifications, and its structure has been fully characterized. All these will be discussed in this chapter together with the optical and electrochemical experiments. The electrochemical experiments were done by Dr. Norma S. Tacconi.

In discussing the optical and electrochemical properties of P_h^{4+} , we recognize that in order for us to understand these properties better, it is important that we also describe its molecular orbitals, the transitions between them, and how they relate to empirical observations. Quantum mechanical approximation is a useful tool in this respect. It also helps to discuss what effects each of the individual components have on the overall properties of P_h^{4+} . And since P_h^{4+} was synthesized as a possible improvement over P_c^{4+} it is only fitting that we compare the optical and electrochemical properties of these compounds as well.

2.2 Experimental

2.2.1 Materials and Measurements

All the reagents and solvents used were of reagent grade and used as received. ^1H NMR spectra were obtained on a JEOL Eclipse 300 MHz and 500 MHz spectrometer. The ESI mass spectra were obtained in the positive ionization mode using a Bear Kodiak 1200 mass spectrometer. All elemental analyses were done on a Perkin-Elmer 2400 CHN analyzer. 1,10-phenanthroline-5,6-dione (phendione),⁵⁴ $\text{Ru}(\text{phen})_2\text{Cl}_2$ (phen = phenanthroline),⁵⁵ and 11-nitrodipyrido[3,2-*a*:2',3'-*c*]phenazine (11-nitrodppz)^{56, 57} were synthesized based on literature procedures.

The UV-Visible spectra were obtained using a Hewlett-Packard HP8453A spectrophotometer. All absorption measurements were taken in a 1-cm quartz or glass cuvette at room temperature. Sample concentration is 16 μM dissolved in MeCN.

Electrochemical data were obtained on a CHI620C electrochemical analyzer (CH Instruments, Austin, TX, USA). A single-compartment, three-electrode electrochemical cell was used with either a glassy carbon (1.5 mm diameter disk) or gold (1.0 mm diameter disk) from

Cypress Systems as working electrode. Immediately before use, the electrode was polished to a mirror finish with wet alumina (Buehler, 0.05 μm), followed by rinsing with Millipore Milli-Q water and sonication. A Pt wire and a non-leak Ag/AgCl, saturated KCl reference electrode (Cypress Systems, model EE009) were used as counter and reference electrodes, respectively. All potentials were measured and are quoted vs. a Ag|AgCl|sat'd.KCl reference electrode. All electrochemical data were recorded in acetonitrile (MeCN) with 0.1 M NBu_4PF_6 as supporting electrolyte. The solvent (MeCN, Aldrich) was dried on alumina and distilled under nitrogen prior to using. The supporting electrolyte Bu_4NPF_6 (Aldrich) was dried overnight under vacuum at 60 $^\circ\text{C}$ and stored under nitrogen. Cyclic voltametry (CV) and differential pulse voltammetry (DPV) were used for the electrochemical characterization of P_h^{4+} .

2.2.2 Synthesis

10,11-Diaminodipyrido[3,2-a:2',3'-c]phenazine (10,11-diaminodppz)

This preparation is a modification of a known literature procedure.⁵⁸ A mixture of 2.00 g (6 mmol) of 11-nitrodppz and 10 g (0.14 mol) of hydroxylaminehydrochloride dissolved in 100 mL ethanol was refluxed under nitrogen. A solution of KOH (20 g) in methanol (100 mL) was then added dropwise during heating. After heating overnight, the mixture was left to stand for about 6 hours, then the precipitate was filtered, washed with water and dried under vacuum to give 1.15 g (54% yield) of the desired compound. ^1H NMR(ppm, DMSO-d_6): 5.59 (s, 2H), 5.62 (s, 2H), 7.51 (s, 2H), 7.85 (m, 2H), 9.07 (dd, $J_1 = 4.1$ Hz, $J_2 = 1.8$ Hz, 1H), 9.11 (dd, $J_1 = 4.5$ Hz, $J_2 = 1.7$ Hz, 1H), 9.38 (dd, $J_1 = 8.1$ Hz, $J_2 = 1.7$ Hz, 1H), 9.79 (dd, $J_1 = 8.1$ Hz, $J_2 = 1.7$ Hz, 1H). MS: m/z 313 (MH^+).

9,12,21,22-Tetraazatetrapyrido[3,2-a:2',3'-c:3''2''-m:2''',3'''-o]pentaphene (tatpp_n)

0.10 g (0.32 mmol) of 10,11-diaminodppz and 0.15 g (0.71 mmol) of phendione (dissolved in minimal amount of chloroform) were added to 25 mL glacial acetic acid and refluxed for 12 hours. The mixture was cooled then filtered. The precipitate was washed with acetic acid, methanol, and chloroform and dried to give 0.03 g (19% yield). ^1H NMR(ppm,

CDCl₃-TFA): 8.40 (dd, J₁ = 8.3 Hz, J₂ = 5.0 Hz, 2H), 8.51 (dd, J₁ = 8.4 Hz, J₂ = 5.1 Hz, 2H), 8.87 (s, 2H), 9.41 (dd, J₁ = 4.8 Hz, J₂ = 1.2 Hz, 2H), 9.44 (dd, J₁ = 5.0 Hz, J₂ = 1.3 Hz, 2H), 10.22 (dd, J₁ = 8.3 Hz, J₂ = 1.3 Hz, 2H), 10.51 (dd, J₁ = 8.1 Hz, J₂ = 1.1 Hz, 2H). MS: *m/z* 487 (MH⁺).

[(phen)₂Ru(tatpp_h)Ru(phen)₂][PF₆]₄·(P_h)[PF₆]₄

A mixture of 0.10 g (0.21 mmol) tatpp_h and 0.26 g (0.49 mmol) Ru(phen)₂Cl₂ were suspended in 30 mL ethanol and 30 mL water and refluxed for 7 days. The mixture was then stored at 4 °C for 12 h and filtered. Addition of aqueous NH₄PF₆ resulted in a precipitate, which was isolated by filtration and washed with 10 mL water (3x) and 10 mL ethanol (3x). The product was further purified by repeated methatheses between Cl⁻ and PF₆⁻ salts. The Cl⁻ salt was prepared from the PF₆⁻ salt by adding a concentrated solution of n-tetrabutylammonium chloride in acetone to a concentrated solution of the PF₆⁻ salt in acetone. The precipitate was filtered and washed with 5 mL acetone (3x) and 10 mL diethyl ether. The Cl⁻ salt was converted back to the PF₆⁻ salt by adding a concentrated solution of ammonium hexafluorophosphate in water to the Cl⁻ salt dissolved in minimum amount of water. The precipitate was filtered and washed with 10 mL water (3x), 10 mL ethanol, and 10 mL diethyl ether. The metathesis was repeated several times until the desired purity was obtained. Actual yield was at 44% (0.18 g). ¹H NMR (ppm, CD₃CN): 7.67 (m, 8H), 7.88 (dd, J₁ = 8.3 Hz, J₂ = 5.4 Hz, 2H), 7.91 (dd, J₁ = 8.4 Hz, J₂ = 5.6 Hz, 2H), 8.06 (m, 4H), 8.22 (m, 4H), 8.29 (d, J = 2.0 Hz, 4H), 8.29 (s, 8H), 8.63 (m, 4H), 8.65 (m, 4H), 8.84 (s, 2H), 9.79 (dd, J₁ = 8.3 Hz, J₂ = 1.0 Hz, 1H), 10.12 (dd, J₁ = 8.3 Hz, J₂ = 1.0 Hz, 1H). MS: *m/z* 1844 ([M+3PF₆]⁺), 850 ([M+2PF₆]²⁺), 518 ([M+PF₆]³⁺), 352 (M⁴⁺). Anal. Calcd. for C₇₈H₄₆N₁₆F₂₄P₄Ru₂: C, 47.09; H, 2.33; N, 11.27. Found: C, 45.37; H, 1.91; N, 10.53.

2.3 Results and Discussion

2.3.1 Synthesis

Our initial attempt to synthesize P_n⁴⁺ was based on the synthetic scheme shown in Figure 2.1 in which the key synthetic precursor, 1,2,3,4-tetraaminobenzene was prepared from 2,4,6-tribromophenol⁵⁹ and tetrasulfur tetranitride (S₄N₄),⁶⁰ via the bromobenzo[1,2-c;3,4-

c']bis[1,2,5]thiadiazole intermediate⁶¹. The principal problem encountered in this route was the difficulty in preparing a sufficient quantity of S₄N₄. The synthesis of this compound was time-consuming, involved a cumbersome experimental set-up, and gave low yields. This route was abandoned in favor of the route shown in Figure 2.2, in which the key intermediate is 10,11-diaminodppz. 11-Nitrodppz was obtained in good yield (87%) via the condensation of 1,2-

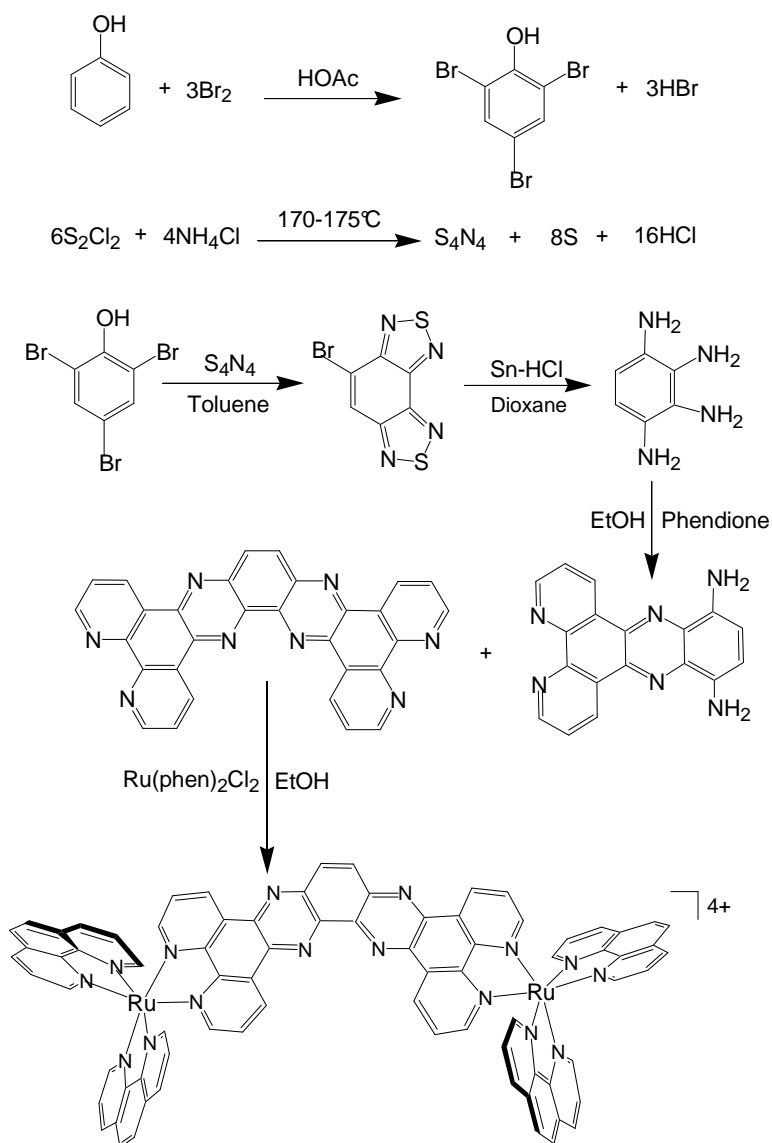


Figure 2.1 Initial synthetic scheme for the synthesis of P_h^{4+} .

diamino-4-nitrobenzene with 1,10-phenanthroline-5,6-dione. We intended to introduce the amino function at the 10th position via a base induced amination reaction to form 10-amino-11-nitrodppz, and then reduce the nitro function to give the desired diamine. Recently, however, Casiraghi et al.⁵⁸ reported that both the amination and reduction reactions can occur in a single reaction pot for the preparation of 1,2-diaminophenazine. Using a slight modification of the Casiraghi procedure, we were able to directly convert 11-nitrodppz to 10,11-diaminodppz in 54% yield. The two sets of reaction conditions are shown in Table 2.1 for comparison. In our case, the more limited solubility of the 11-nitrodppz required a greater overall reaction volume, and longer reaction times at reflux. We also made a switch from ethanol to methanol in preparing the alcoholic KOH solution because of the base's greater solubility in methanol.

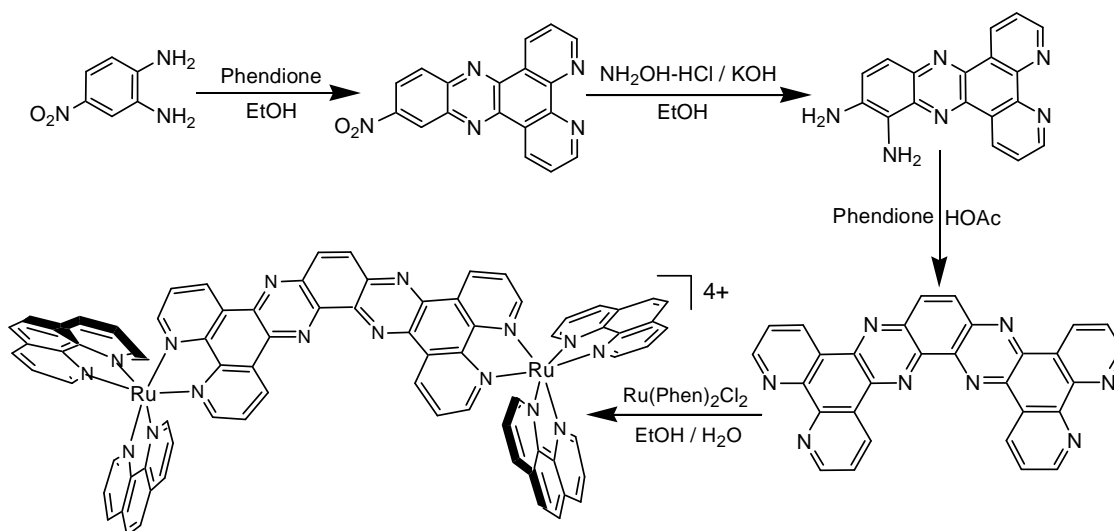


Figure 2.2 Second synthetic scheme for the synthesis of P_h^{4+} .

As shown in Figure 2.2, the reaction of 10,11-diaminodppz with 1,10-phenanthroline-5,6-dione yielded the desired ligand, tatpp_h. This free ligand, like tatpp_c, is only sparingly soluble in most common organic solvents and precipitates from solution upon forming, and can be purified by extensive washing with common solvents.

The ruthenium dimer, P_h^{4+} , is prepared in 44% yield by refluxing a suspension of tatpp_h with 2.1 equivalents of Ru(phen)₂Cl₂ in 1:1 ethanol-water for 7 days.

Table 2.1 Reaction conditions for the synthesis of P_h^{4+} modified vs. original procedure.⁵⁸

Starting Material / Product	Starting Material	NH ₂ OH·HCl	Alc. KOH	Alcohol	Conditions	Yield
1,2-diaminophenazine / 2-nitrophenazine ^a	1.0 g (4 mmol)	2.5 g (0.04 mol)	30 mL (0.17 g/mL) in EtOH	25 mL EtOH	60-65°C 4 h.	75%
11-nitrodppz / 10,11-diaminodppz	2.0 g (6 mmol)	10 g (0.14 mol)	100 mL (0.20 g/mL) in MeOH	100 mL MeOH	reflux overnight	54%

2.3.2 Structural Characterization

The structure of 10,11-diaminodppz was confirmed by ¹H NMR spectroscopy and ESI-mass spectrometry. The proton peaks in the ¹H NMR spectrum of 10,11-diaminodppz were assigned as shown in Figure 2.3 and is consistent with the proposed structure. Assignments were made by analysis of the chemical shifts, hyperfine coupling and by comparison with the closely related analogues, 11,12-diaminodppz⁵⁷ and dppz. Unlike these two analogues, 10,11-diaminodppz has lower symmetry along its long axis and thus we observe two sets of coupled peaks for the H_a, H_b, H_c and H_a' ,H_b' ,H_c' spin systems. Surprisingly, the two protons at positions H_d and H_e, which are not magnetically equivalent, appear as a single peak at 7.51 ppm which complicated the assignment. Importantly, mass spectrometric data showed a single parent ion peak at 313 m/z which matches the expected value for the monoprotonated diamine species [M+H]⁺. Lastly, the structure is confirmed by its successful use as a diamine in the preparation of tatpp_h in the subsequent reaction with 1,10-phenanthroline-5,6-dione.

The ¹H NMR spectrum of tatpp_h was obtained in a mixture of CDCl₃ and TFA which appears to solubilize the ligand but may not fully prevent aggregation in solution. As seen in Figure 2.4 the spectrum of this solution shows a poor baseline and peak shape which we suspect is a consequence of aggregation. Nonetheless, the spectrum is resolved well enough to

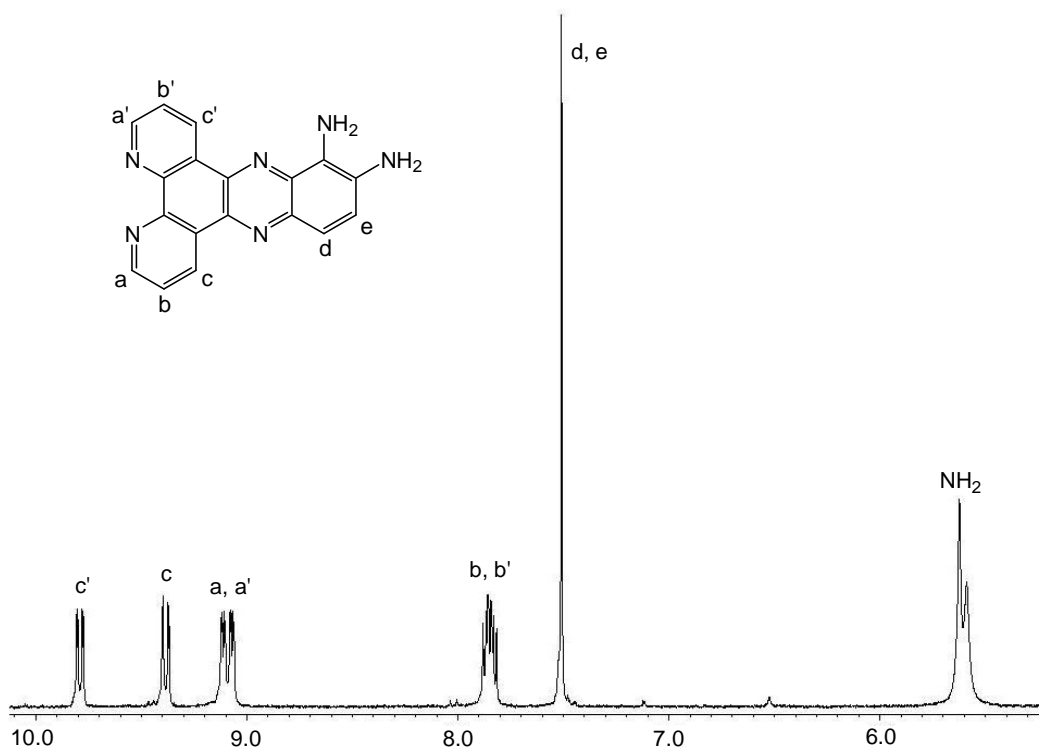


Figure 2.3 ¹H NMR spectrum of 10,11-diaminodppz in DMSO-d₆.

help with structural characterization. The tatpp_h ligand has C_{2v} point group symmetry and should show 7 distinct peaks – all of which are observed in this spectrum and assigned as indicated in Figure 2.4. As expected two AMX coupled spin systems are seen corresponding to the phenanthroline outer (H_a , H_b , H_c) and inner ($H_{a'}$, $H_{b'}$, $H_{c'}$) hydrogens. A COSY spectrum was obtained to determine which peaks were correlated. The two hydrogens (H_d) on the central benzene ring are symmetrically equivalent and appear as a singlet at 8.87 ppm. The downfield shift is typical of hydrogens adjacent to pyrazine-like nitrogens in these compounds. The linear ligand tatpp_c is even more symmetric (D_{2h} point group symmetry), and shows a total of 4 peaks with the central H_d hydrogens shifted even further downfield at 9.79 ppm due to the positioning between two aza nitrogens.¹⁹ In addition to the NMR data, the ESI-MS data showed a monoprotonated parent ion peak $[M+H]^+$ at 487 m/z which is the expected value for tatpp_h.

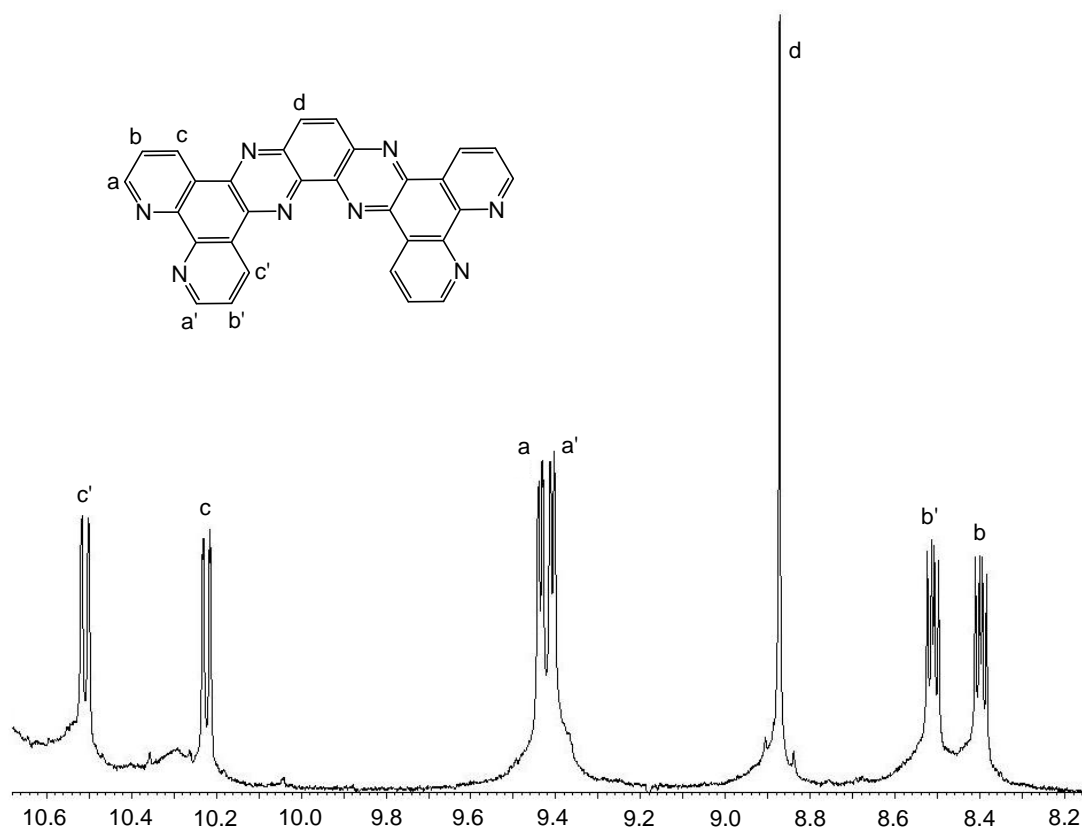


Figure 2.4 ^1H NMR spectrum of tatpp_h in CDCl_3 -TFA.

Coordination of two $[\text{Ru}(\text{phen})_2]^{2+}$ fragments to tatpp_h give the dinuclear complex P_h^{4+} which is freely soluble in MeCN as the hexafluorophosphate salt and in water as the chloride salt. The method of preparation does not control the absolute stereochemistry at the two Ru(II) chiral centers and thus the product is actually a mixture of diastereomers, $\Delta\Delta$, $\Lambda\Lambda$, and $\Lambda\Delta$. As has been seen with similar dinuclear complexes of tpphz , tatpp_c and tatpq ,⁶²⁻⁶⁶ these diastereomers have identical NMR spectra owing to the large distance between stereocenters.¹⁹ Since only one set of NMR signals are seen, the interpretation of the ^1H NMR spectrum is straightforward and has been assigned using a combination of COSY data and by comparison with related compounds (e.g. P_c^{4+}). As indicated in Figure 2.5, peaks associated with the phen ligands are labeled 1 through 8 and while peaks associated with tatpp_h are given a letter designation. Only seven peaks are observed with the tatpp_h ligand because all of the

diastereomers possess either two-fold rotation or mirror plane symmetry elements through the center of the tatpp_h ligand. All of these peaks are shifted upfield in the complex relative to the free ligand, with H_a and H_{a'} showing the largest shift ($\Delta\delta \sim 1.2$ ppm), presumably due to the proximity to the Ru(II) centers.

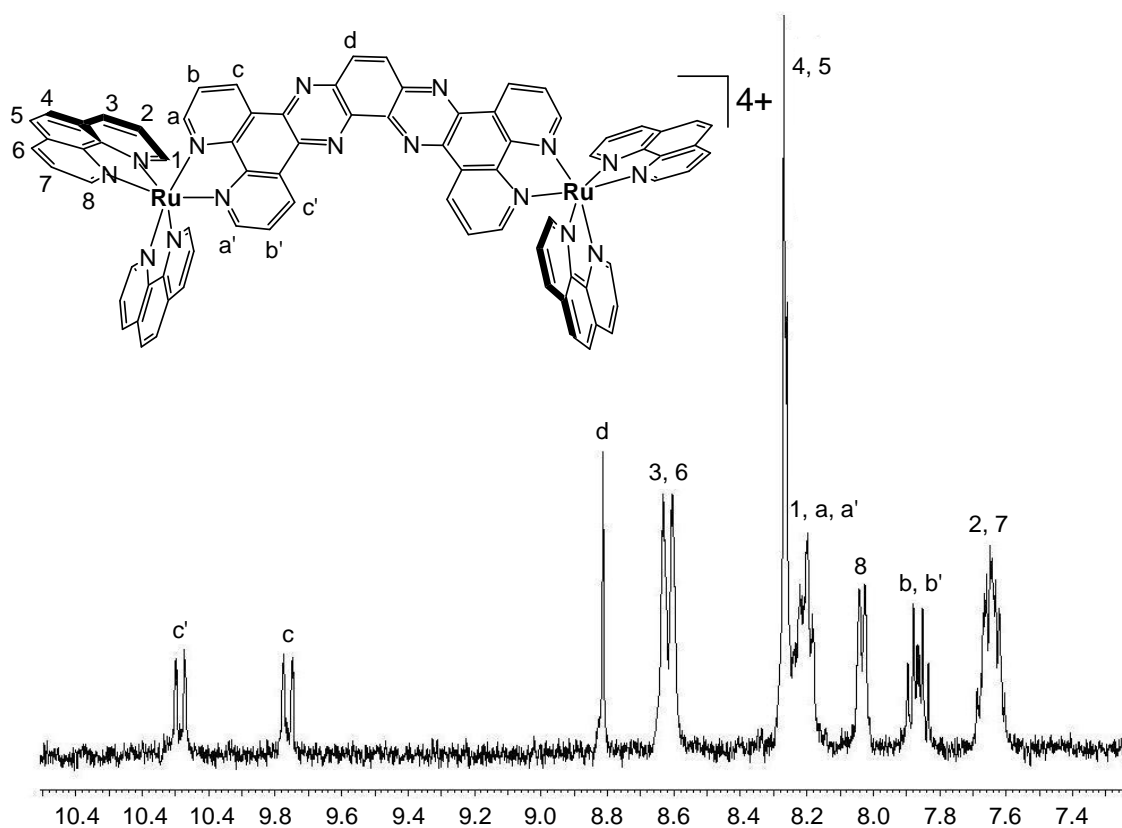


Figure 2.5 ^1H NMR spectrum of P_h^{4+} in CD_3CN .

Compared to P_c^{4+} , the biggest changes in the spectrum of P_h^{4+} are: 1. the appearance of three new peaks as H_{a'}, H_{b'} and H_{c'} which are no longer equivalent to H_a, H_b, and H_c; and 2. the downfield chemical shift of the two central H_d hydrogens is considerably less for P_h^{4+} ($\Delta\delta \sim 0.9$ ppm), as these hydrogens are only adjacent to one aza nitrogen each in P_h^{4+} compared to two each in P_c^{4+} . The ESI-MS spectrum for P_h^{4+} , shown in Figure 2.6, is consistent with the following parent ions: $[\text{P}_h+3\text{PF}_6]^+$ at 1843 m/z, $[\text{P}_h+2\text{PF}_6]^{2+}$ at 850 m/z (the highest peak),

$[\text{P}_h + \text{PF}_6]^{3+}$ at 518 m/z, and P_h^{4+} at 352 m/z. These data in conjunction with the elemental analyses and NMR data prove the structure of the complex.

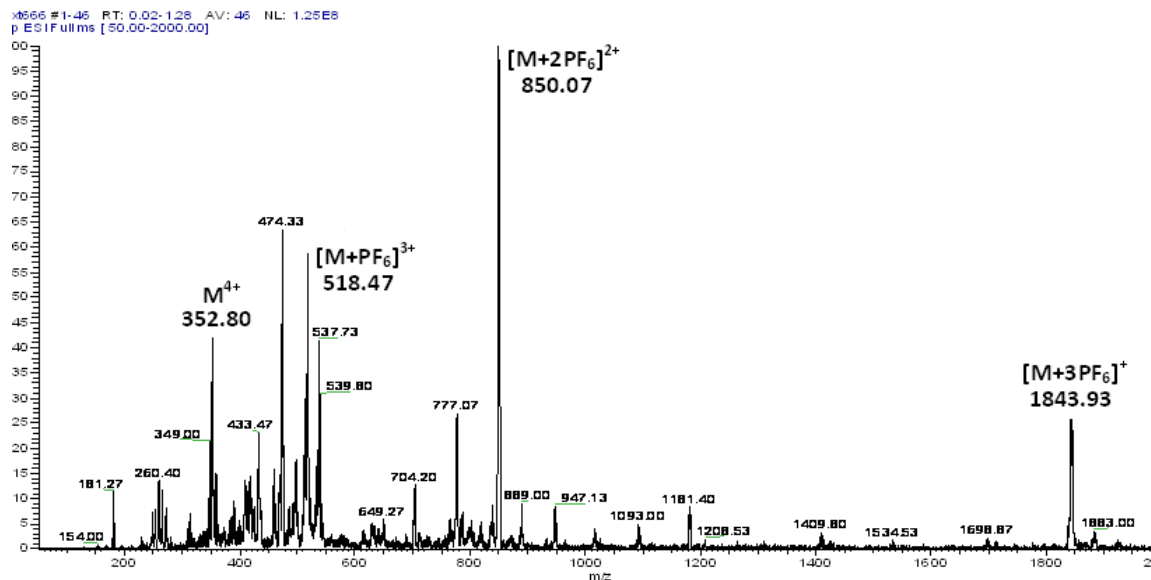


Figure 2.6 ESI-MS spectrum of the complex P_h^{4+} .

2.3.3 Electronic Spectra

The absorption spectra of the ligands, tatpp_h and tatpp_c , in MeCN are shown in Figure 2.7a and the spectra of the corresponding ruthenium dimers, P_h^{4+} and P_c^{4+} , are shown in Figure 2.7b. As the free ligands are insoluble in this solvent, a 10 fold molar excess of $\text{Zn}(\text{BF}_4)_2$ was added to each solution to complex and solubilize the ligand. While Zn(II) coordination may slightly perturb some ligand-centered (LC) transitions, it is not expected to add any transitions to the overall spectrum in the region shown.³⁵ Both tatpp_c and tatpp_h have sharp, intense absorption bands in the 300 to 400 nm region. Given the intensity and sharpness of the absorptions, these are assigned as $\pi-\pi^*$ transitions.⁶⁷ For the tatpp_c ligand, the band peaks at 323 nm ($\epsilon = 46,200 \text{ M}^{-1}\text{cm}^{-1}$) whereas for tatpp_h , the peak is found at 358 nm ($\epsilon = 57,000 \text{ M}^{-1}\text{cm}^{-1}$). Weaker, but still moderately intense absorptions are observed at 448 ($\epsilon = 17,400 \text{ M}^{-1}\text{cm}^{-1}$) and 442 nm ($\epsilon = 1,900 \text{ M}^{-1}\text{cm}^{-1}$) for tatpp_c and tatpp_h , respectively. However, these bands differ

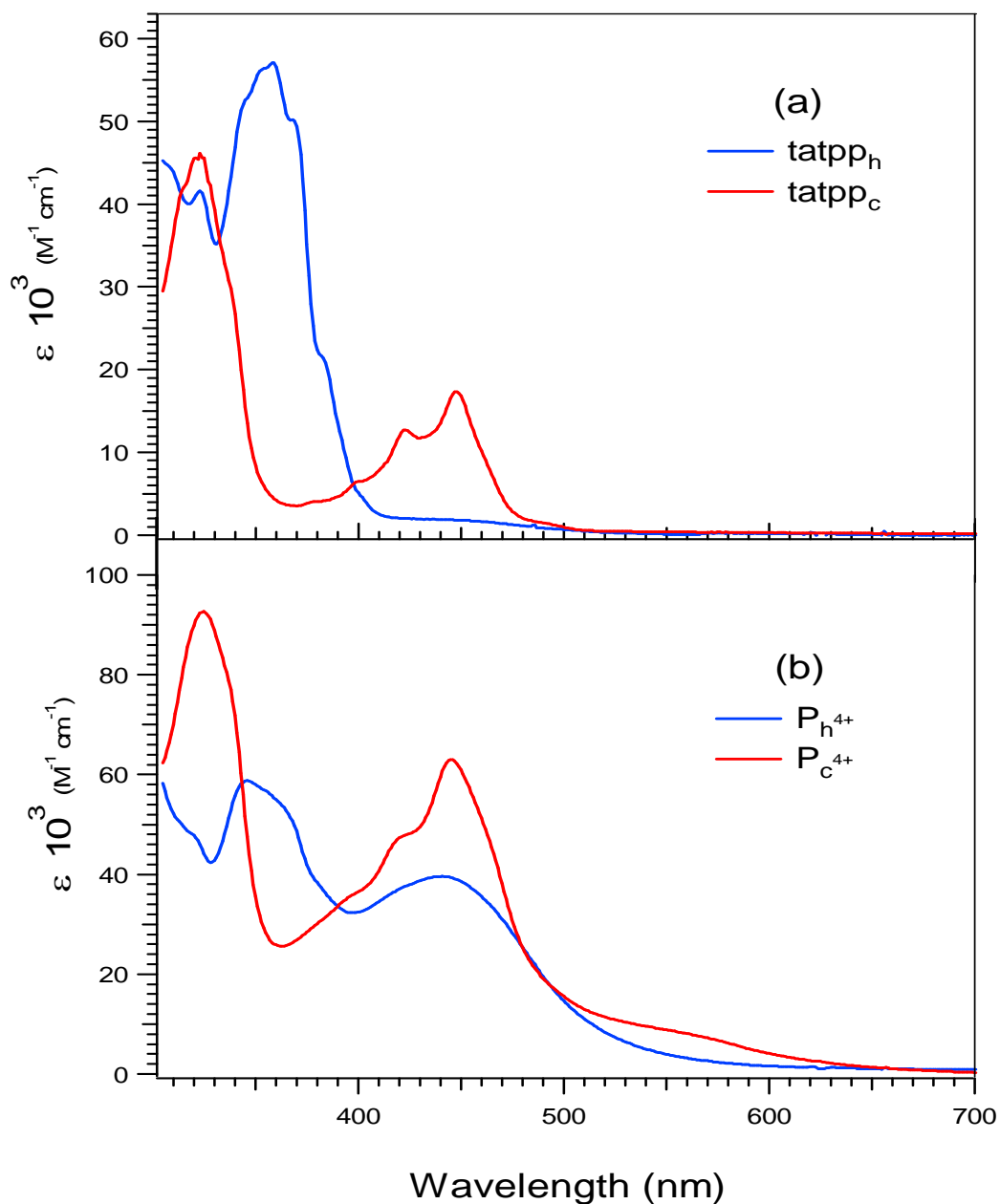


Figure 2.7. UV-Vis spectra of (a) tatpp_h and tatpp_c and (b) P_h^{4+} and P_c^{4+} . All spectra were obtained in MeCN at room temperature with a sample concentration of 16 μM . tatpp_h and tatpp_c were solubilized with excess Zn(II) ions.

significantly in shape and intensity from one another. For tatpp_c , this long wavelength band is more intense and shows vibronic structure with overtones at 423 and 448 nm. For tatpp_h , the band is approximately 10-fold less intense and is broad and featureless. The exact nature of

these transitions are unclear and the modest intensity suggests possibly $n-\pi^*$ transition in tatpp_h ,⁶⁷ however $\pi-\pi^*$ is not ruled out. Again, as the Zn(II) ion is not expected to add to the absorption spectrum in this region, all of these transitions are assigned as LC bands.

Upon coordination to two $[\text{Ru}(\text{phen})_2]^{2+}$ fragments, the absorption spectra of both \mathbf{P}_c^{4+} and \mathbf{P}_h^{4+} show a new broad and intense absorption band around 440 nm which is assigned as the MLCT band typical of the $[\text{Ru}(\text{phen})_3]^{2+}$ subunit. In \mathbf{P}_c^{4+} , we have demonstrated that the absorption spectrum can be viewed largely as a summation of the individual molecular components, thus indicating weak electronic coupling between components.⁴¹ The partially structured broad absorption peaking at 445 nm is the additive spectra of two $[\text{Ru}(\text{phen})_3]^{2+}$ MLCT bands plus the structured LC absorption for tatpp_c in the same region. The UV peak at 325 nm is largely just the tatpp_c LC band in the same region. The only new peaks seen in the spectrum of \mathbf{P}_c^{4+} that are noticeable are a significant shoulder at 565 nm and a weaker peak at 960 nm. As these peaks show moderate extinction coefficients ($\epsilon = 7,700$ and $900 \text{ M}^{-1}\text{cm}^{-1}$ respectively), it is clear they are not simply d-d transitions. At this time, their electronic nature is still speculative.

Assuming similar weak electronic coupling between molecular components in \mathbf{P}_h^{4+} , we can break down its absorption spectrum as two $[\text{Ru}(\text{phen})_3]^{2+}$ MLCT bands plus the broad unstructured LC absorption in the same region giving rise to the peak at 441 nm. The intense UV peak at 346 nm would largely be a LC band for the tatpp_h ligand. Unlike \mathbf{P}_c^{4+} , there are no lower energy bands observed in \mathbf{P}_h^{4+} .

For compounds like \mathbf{P}_c^{4+} and \mathbf{P}_h^{4+} , and their bridging ligands tatpp_c and tatpp_h respectively, it is helpful to explain their optical and redox properties by a localized molecular orbital description in which the different excited and redox states are treated as being localized on specific parts of the molecule. This type of localized MO approximation has been very helpful in explaining the electrochemical and photophysical properties of related ruthenium(II) tpphz ^{63, 68-72} and dppz complexes.^{56, 73} For example, dppz has been described as having two

energetically similar acceptor orbitals which are predominantly localized on the 'bpy-like' and 'phenazine-like' portions of the ligand. A MLCT excitation in $[(\text{phen})\text{Ru}(\text{dppz})]^{2+}$ is best explained as promotion of a Ru ($d\pi$) electron to the 'bpy-like' MO on dppz, even though this orbital is higher in energy than the 'phenazine-like' MO. However, electrochemical reduction of this complex first populates the 'phenazine-like' MO and thus the redox behavior is not exactly correlated with the optical behavior.

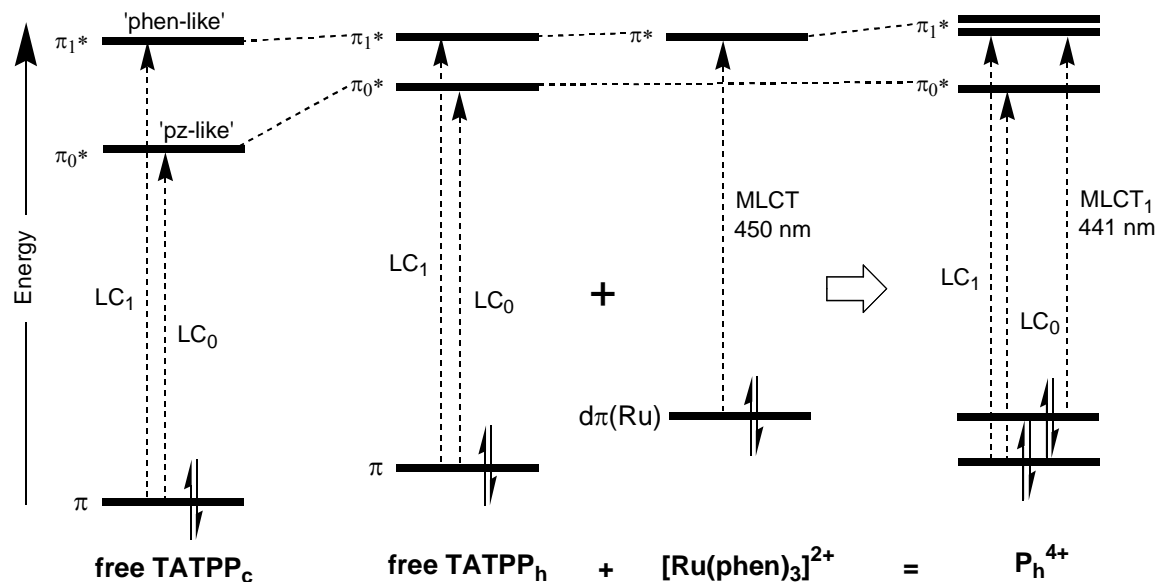


Figure 2.8 MO energy diagram of tatpp_h , $[\text{Ru}(\text{phen})_3]^{2+}$, and P_h^{4+} .

To help understand the spectra in Figure 2.7, we have developed a partial MO diagram, shown in Figure 2.8, based on MO calculations of the free ligand using the PM3 method. While these calculations utilize a relatively simple basis set and do not include the ruthenium ions or peripheral phen ligands, they do reveal the relevant ligand-centered donor (HOMO) and acceptor (LUMO and LUMO+1) orbitals of tatpp_c and tatpp_h . The energy of these orbitals will change upon coordination, however, the relative ordering and energies are unlikely to be significantly altered.

As seen on the far left in Figure 2.8, the two electronic transitions at 448 and 323 nm in tatpp_c can be assigned as the $\pi_{\text{HOMO}}-\pi_0^*$ transition (LC_0) and the $\pi_{\text{HOMO}}-\pi_1^*$ transition (LC_1),

respectively. In tatpp_h , these transitions occur at 442 nm (LC_0) and 358 nm (LC_1) respectively and thus the energy levels in Figure 2.8 (second from the left) are adjusted to reflect this. The third MO diagram from the left, Figure 2.8, shows the two orbitals involved in the Ru ($d\pi$)-phenanthroline (π^*) MLCT typical of $[\text{Ru}(\text{phen})_3]^{2+}$ and related compounds. This transition is usually seen as a broad absorption peaking between 400 to 500 nm. The final MO diagram in Figure 2.8 (right) is for P_h^{4+} and shows the combination of the LC transitions for tatpp_h and the MLCT transition.

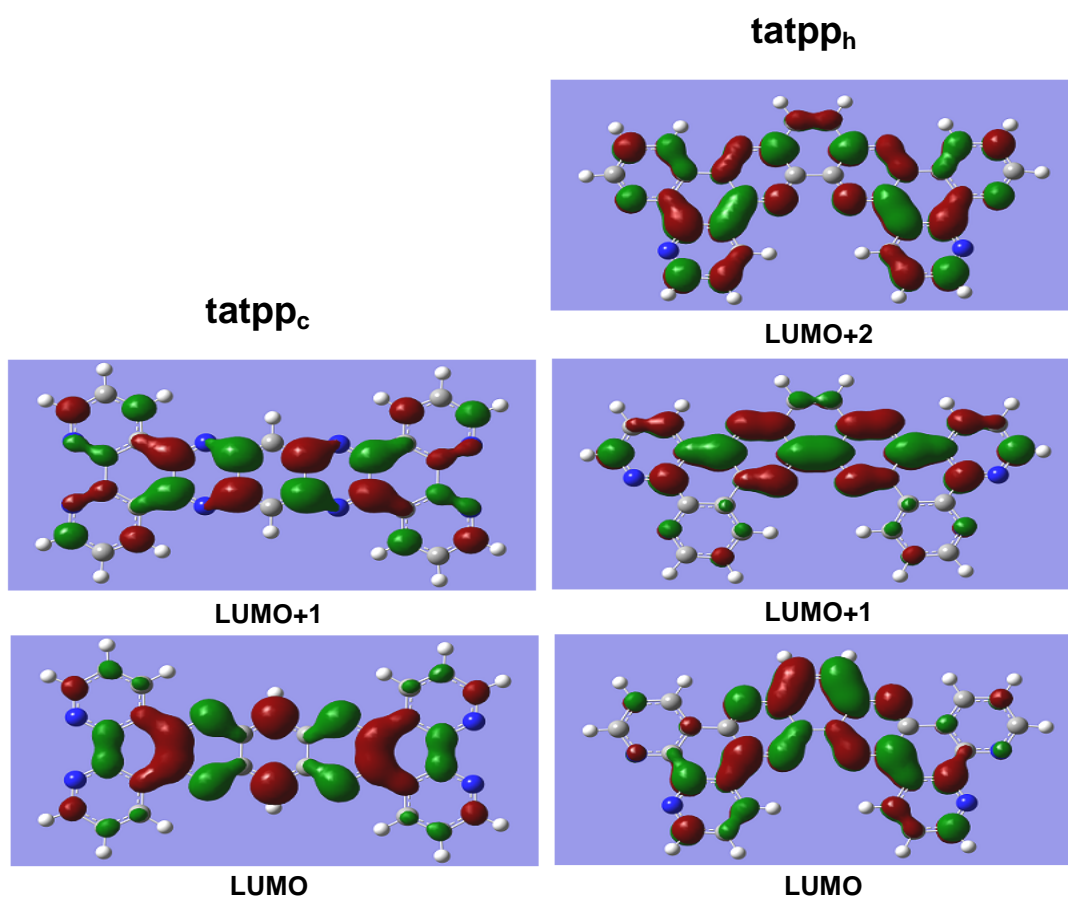


Figure 2.9 MO pictures for the relevant orbitals of tatpp_h and tatpp_c .

As shown in Figure 2.9, the LUMO and LUMO+1 for tatpp_c can be described as having orbital density localized on the 'phen-like' and 'pyrazine-benzene-pyrazine' (or for simplicity 'pz-like') portions of the ligand, respectively. Even if this description is only partially accurate, the

LUMO+1 has the same electron distribution and symmetry as the LUMO (acceptor orbital) in phenanthroline and thus is the orbital which is most likely populated upon excitation of the MLCT. On the other hand, the tatpp_c LUMO has little orbital density on the nitrogens directly coordinated to the Ru(II) centers and thus has poor overlap with the Ru (d π) orbitals. Here the orbital density is localized on the central portion of the ligand. We postulate that direct excitation of the Ru (d π) electron into the tatpp_c LUMO is not observed (or has a low transition probability) due to this poor coupling. Indirect evidence of this is the observation of the MLCT maxima at ~ 445 nm for **P_c⁴⁺**, which is nearly identical to the maxima for [Ru(phen)₃]²⁺. Both orbital calculations and electrochemical data indicate that the LUMO is much lower in energy in tatpp_c than in phen and therefore we would expect a lower energy peak if the Ru (d π)-tatpp_c LUMO MLCT were observed. In fact, it is possible that the modest peak seen at 960 nm in **P_c⁴⁺** is this transition.

As seen in Figure 2.9, the symmetry and orbital density distribution for the LUMO, LUMO+1, and LUMO+2, in tatpp_h are different from tatpp_c, however, a similar argument regarding the electronic spectrum of **P_h⁴⁺** seems to hold. The MLCT in **P_h⁴⁺** from the Ru (d π) orbital into the tatpp_h LUMO is apparently weak or absent as no new transitions are observed at energies below 450 nm. The tatpp_h LUMO+1 and LUMO+2 are close in energy and either could be the predominant acceptor (or 'phen-like') orbital for MLCT in **P_h⁴⁺**. This MO picture is simplified in Figure 2.8 (right) where the π_1^* orbital is meant to represent whichever of these two MOs (LUMO+1 or LUMO+2) is the relevant acceptor orbital.

2.3.4 Electrochemistry

Representative cyclic voltammograms (CVs) for the electroreduction of complex **P_h⁴⁺** are shown in Figure 2.10, while the oxidation process of the ruthenium moiety is presented as an inset located at its left top corner. For the electroreduction processes, three CVs were recorded from the system open circuit potential and down to progressively more negative switching potentials of -1.10 V, -1.30 V and -1.42 V respectively. These CVs allow us to easily

deconvolute the three successive reductive processes observed in P_h^{4+} that are indicated as C_I/A_I , C_{II}/A_{II} , and C_{III}/A_{III} (C standing for cathodic and A for anodic processes respectively) in Figure 2.10. The detection of peak C_{II} is clearly depicted in the second cyclic voltammogram due to its switching potential avoiding the contribution of the third C_{III} process. As the third voltammogram spans down to -1.42 V, process C_{III} takes place and the related oxidation peak A_{III} masks the underlying A_{II} peak due to the proximity of both peaks. Effectively, each individual CV in Figure 2.10 brought about the detection of a single redox couple (i.e., correlated cathodic and anodic peaks). The first redox process, characterized as C_I/A_I , shows up with a half-wave potential, $E_{1/2}$, of -0.73 V vs Ag/AgCl; the second C_{II}/A_{II} redox process is observed at $E_{1/2} = -1.16$

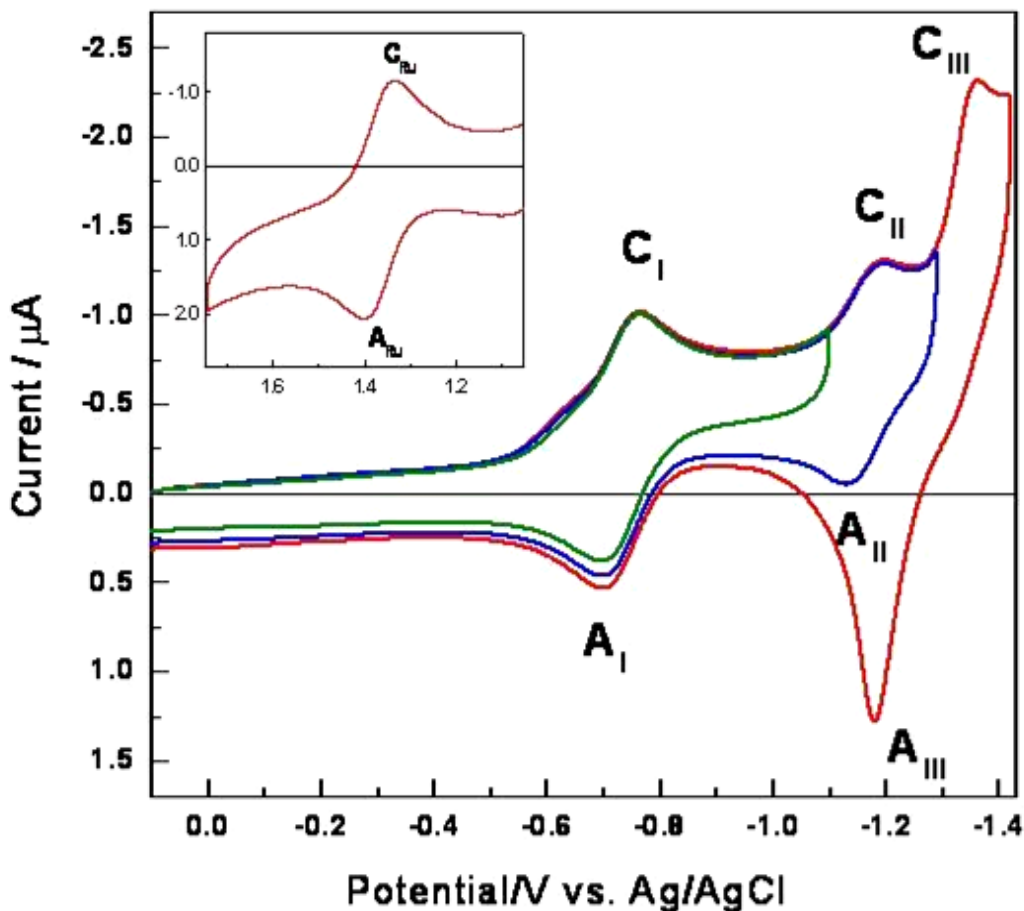


Figure 2.10 Cyclic voltammograms for 20 μM P_h^{4+} in MeCN containing 0.1 M TBAPF₆.

V; and the third process is located at $E_{1/2} = -1.27$ V. Finally, the inset in Figure 2.10 shows a CV encompassing the potential region corresponding to the $\text{Ru}^{3+/2+}$ redox process in complex P_h^{4+} ($E_{1/2} = 1.36$ V).

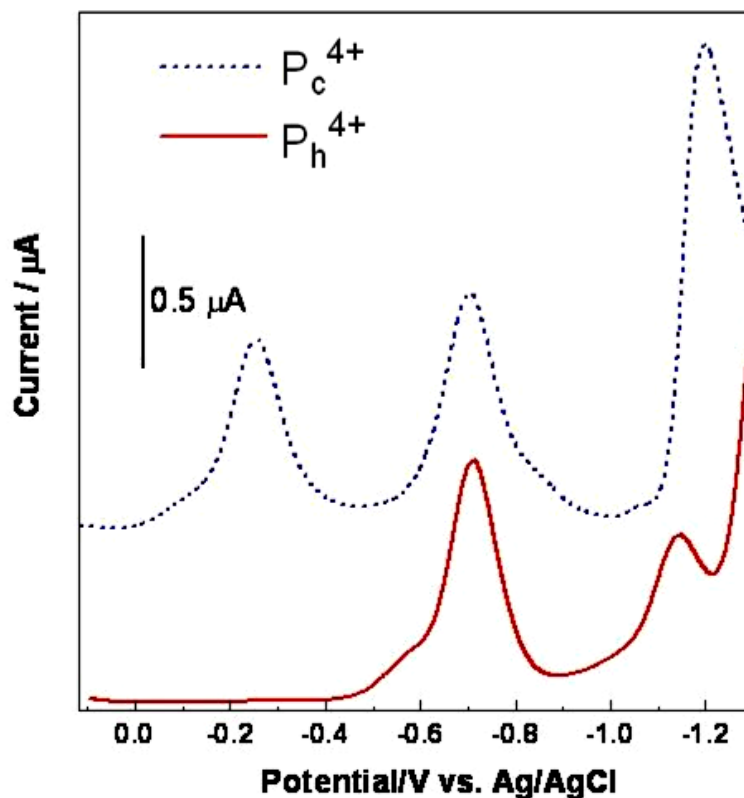


Figure 2.11 Differential pulse voltammograms comparing the electroreduction of P_h^{4+} (solid red line) and P_c^{4+} (dash blue line) in MeCN containing 0.1 M TBAPF₆. Potential pulse amplitude = 0.05 V, step size = 0.004 V, pulse duration = 0.05 s, pulse period = 0.2 V.

The first two redox processes in Figure 2.10, C_I/A_I and $\text{C}_{II}/\text{A}_{II}$, have been shown to be diffusion-controlled reversible processes.⁷⁴ Specifically, the peak separation ΔE for the first two processes is 59 mV which are diagnostic for reversible 1-electron processes,

$$\Delta E = E_{\text{PCx}} - E_{\text{Px}} = 59.0/n \text{ mV} \quad (2.1)$$

where n is the number of electrons involved in the process,. Furthermore, the I_C/I_A ratio between cathodic (I_C) and anodic (I_A) current peaks should be equal to 1 for a reversible process and is

seen here. The third process, C_{III}/A_{III} , does not behave as ideally and is considered quasi-reversible. The ΔE for this process is 178 mV and is indicative of a 2 or 3-electron process.

To finish the electrochemical characterization of \mathbf{P}_h^{4+} , Figure 2.11 compares DPV runs for the electroreduction of \mathbf{P}_h^{4+} and its analog \mathbf{P}_c^{4+} ; the latter complex was thoroughly studied in our group.^{34, 75, 76} Both runs were performed under the same experimental conditions in MeCN containing 0.1 M TBAPF₆ media and in the potential range from -0.05 to -1.3 V (i.e. using the potential window as in Figure 2.10). These two dinuclear complexes differ only in the central ligand: $tatpp_h$ for \mathbf{P}_h^{4+} and $tatpp_c$ for \mathbf{P}_c^{4+} , both having phenanthroline as terminal ligands.

Three successive electroreduction processes are seen for \mathbf{P}_c^{4+} while only two are depicted for \mathbf{P}_h^{4+} . For complex \mathbf{P}_c^{4+} , the three well-separated waves (Figure 2.11 blue dash line) are associated with the electroreduction of the central $tatpp_c$ ligand by two successive one-electron redox process ($tatpp_c^0/tatpp_c^{-1}$, $tatpp_c^{-1}/tatpp_c^{-2}$) followed by a two-electron reduction ($tatpp_c^{-2}/tatpp_c^{-4}$).^{75, 76} Contrastingly, two main peaks are seen in the electroreduction of complex \mathbf{P}_h^{4+} (Figure 2.11 red solid line) in the same potential window. These data plus the potentials for the $Ru^{3+/2+}$ couple are collected in Table 2.2, in which potentials are reported both as collected relative to Ag/AgCl and to the normal hydrogen electrode (NHE). Equation 2.2 was used to obtain $E_{1/2}$ from the DPV runs:

$$E_c = E_{1/2} - \Delta P/2 \quad (x = 1 \text{ or } 2) \quad (2.2)$$

where E_c is the cathodic peak potential and ΔP is the DPV pulse amplitude (i.e.; 50 mV for data in Figure 2.11).⁷⁷

The C_I/A_I couple in complex \mathbf{P}_h^{4+} occurs at a considerably more negative potential (-0.53 V vs NHE) than was observed for the first reductive couple in \mathbf{P}_c^{4+} (-0.02 V vs NHE). We associate this redox process with a one-electron reduction of the $tatpp_h$ ligand ($tatpp_h^{0/-1}$) in the complex \mathbf{P}_h^{4+} . Similarly, the second reductive process, C_{II}/A_{II} , is associated with a one-electron reduction of the $tatpp_h$ ligand ($tatpp_h^{-1/-2}$) and is also observed to occur at potentials more negative (-0.96 V vs. NHE) than seen for the related process in \mathbf{P}_c^{4+} (-0.51 V vs NHE).

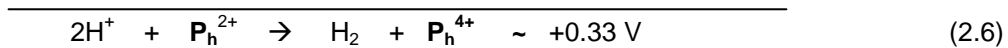
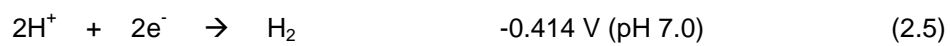
Table 2.2 Redox potentials for the complexes \mathbf{P}_h^{4+} and \mathbf{P}_c^{4+} .

Complex	Reduction (V) ^a Ag/AgCl (NHE)		Oxidation (V) ^a Ag/AgCl (NHE)
	1 st	2 nd	Ru ^{3+/2+}
\mathbf{P}_c^{4+}	-0.22 (-0.02)	-0.71 (-0.51)	1.36 (1.56)
\mathbf{P}_h^{4+}	-0.73 (-0.53)	-1.16 (-0.96)	1.36 (1.56)

^a Potentials were obtained from CV and DPV measurements performed in MeCN containing 0.1 M TBAPF₆.

We can now integrate the electrochemical data into the MO description of the acceptor ligands of \mathbf{P}_c^{4+} and \mathbf{P}_h^{4+} provided in Figures 2.8 and 2.9. As with dppz, we anticipate that electroreduction of these complexes first populates the LUMO of each ligand, whereas the optical properties for the MLCT transition depend principally on the LUMO+1. The reduction potentials reveal the relative energy levels of the ligand-based LUMO's in \mathbf{P}_c^{4+} and \mathbf{P}_h^{4+} as seen in Figure 2.8. Complex \mathbf{P}_h^{4+} requires greater reduction potentials (more negative values) to populate the LUMO in tatpp_h with one and then a second electron (at -0.53 and -0.96 V vs NHE) compared to the same two processes (at -0.02 and -0.51 V vs NHE) in \mathbf{P}_c^{4+} . As indicated in Figure 2.8, the LUMO (π_0^*) in free tatpp_h is shown as being higher in energy than the LUMO (π_0^*) in tatpp_c. The same results were obtained for the coordinated ligands, calculated using the DFT method. As these processes are reversible, the reverse reactions, 0.53 and 0.96 V, occur at considerably higher potentials and therefore provide more driving force for coupling to endogonic reactions like the hydrogen evolving reaction (HER, Equation 2.5). More simply put, upon two-electron reduction, complex \mathbf{P}_h^{4+} stores approximately 1 eV more energy in the bridging ligand than complex \mathbf{P}_c^{4+} . Not only is \mathbf{P}_h^{4+} storing more energy, but by storing 2 electrons, this complex is poised to drive endogonic, multi-electron reductions, such as the HER. As seen by combining Equations 2.3, 2.4 and 2.5, the net chemical reaction shown in

Equation 2.6 is exergonic (ΔG) by -64 kJ/mol! The same sequence of reactions with P_c^{2+} and H^+ to give P_c^{4+} and H_2 is endogonic by +29 kJ/mol.



CHAPTER 3

PHOTOCHEMICAL AND CHEMICAL SPECIATION OF $[(\text{phen})_2\text{Ru}(\text{tatppn})\text{Ru}(\text{phen})_2]^{4+}$

3.1 Introduction

The thermodynamics and kinetics of a photochemical reaction are affected by too many factors that even with adequate preliminary experimental data, one cannot predict with certainty the final course of the reaction. Photochemical experiments simulating real conditions are the only true test of whether a photochemical reaction will actually work. However, experimental data such as optical and electrochemical data can give clues as to the probability of it working, and can give valuable information about the photochemical reaction itself.

In the previous chapter, we showed that \mathbf{P}_n^{4+} absorbs in the visible region and that electrochemically, it can undergo 2 successive 1-electron reductions at much more negative potentials than \mathbf{P}_c^{4+} . In this chapter, we will examine the photochemistry of \mathbf{P}_n^{4+} to determine if it can be photoreduced by 2 electrons. We will also discuss the chemical reduction experiment which will help us identify the species formed in the photochemical process.

3.2 Experimental

All experiments were typically conducted in a sealed, ~3.5 mL quartz or glass cuvette ($b = 1$ cm) and the samples were irradiated using a 150 W halogen lamp (StockerYale Imagelite Model 21AC) or a Philips 150 W, clear glass, incandescent light bulb. These light sources were used interchangeably. For experiments using the incandescent light bulb, the cuvettes were partly immersed in a water bath during irradiation to maintain the samples at room temperature. Absorption spectra were obtained on a Hewlett-Packard HP8453A spectrophotometer.

For the photochemical experiments, a 25-mL solution with 16 μM of sample and 0.25 M of sacrificial reducing agent was prepared and approximately 3-mL aliquots were taken for final

measurement in which the solution was degassed for 10 to 20 min with nitrogen before irradiation.

Preparation of solutions for the chemical reduction of P_h^{4+} was performed inside a glovebox under nitrogen atmosphere. Thoroughly degassed MeCN was used as the solvent and the final concentration of P_h^{4+} in all these experiments was 16 μM . The sample weights used to prepare the stock solutions ranged from 1 mg to as much as 5 mg. The dilutions were then based on the recorded weight. For the reducing agent, a freshly prepared stock solution of cobaltocene containing 1 reducing equivalent per 200 μL of the solution was prepared. An aliquot of the sample stock solution with a typical volume of 400 μL and concentration of 0.12 mM P_h^{4+} was added to five separate cuvettes. After addition of the sample, 0, 1, 2, 3, and 4 equivalents of cobaltocene were separately added to these cuvettes and were diluted to 3 mL. The cuvettes were tightly sealed and were taken out of the glovebox for absorbance measurements. The following day, with the cuvettes still sealed, the absorbance measurements were repeated.

3.3 Results and Discussion

3.3.1 Photoreduction of $[(\text{phen})_2\text{Ru}(\text{tatpp}_h)\text{Ru}(\text{phen})_2]^{4+}$ in MeCN

Visible light irradiation of complex P_h^{4+} in the presence of TEA causes two sequential changes to the absorption spectrum of the solution, as shown in Figure 3.1. The first process, shown in Figure 3.1a, occurs very quickly (after $\sim 2\text{s}$ irradiation) at room temperature and leads to a bleaching of the UV peak at 346 nm and the corresponding appearance of a new very broad absorption centered at 918 nm. In addition, the broad featureless band at 441 nm is seen to increase in intensity and red shifts to 460 nm. Two new shoulders at 500 and 556 nm are also now apparent. Despite the speed of this first process, it is undoubtedly a photochemical process as no changes to the initial spectrum are seen until the sample is irradiated. If air is introduced into the cuvette, we observe a complete regeneration of the starting spectrum, showing the first photochemical process is reversible.

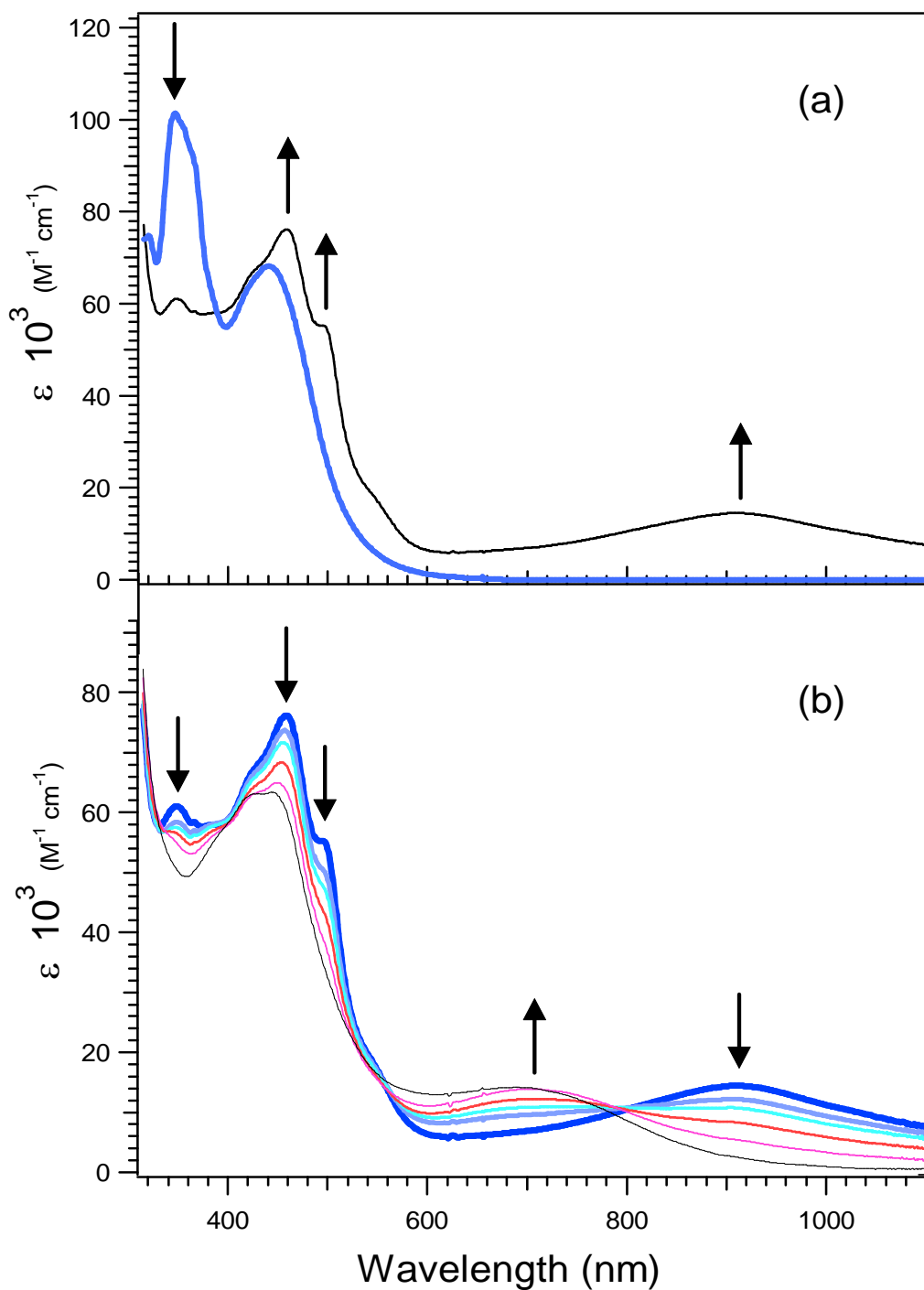
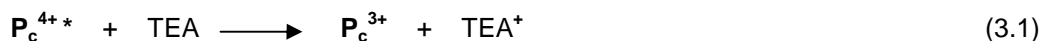


Figure 3.1 Evolution of the absorption spectra of P_h^{4+} during photoirradiation in dry, degassed MeCN ($16 \mu M P_h^{4+}$, $0.25 M TEA$, $150 W$ tungsten bulb, $20^\circ C$) after (a) 2 s irradiation (b) during subsequent periodic measurements over a 30 min period of irradiation.

If we continue to irradiate this sample, a second photochemical process is observed albeit at a much slower rate, requiring approximately 30 min irradiation to reach the final spectrum. As seen in Figure 3.1b, the most noticeable change is the bleaching of the broad peak at 918 nm and a concurrent appearance of a new absorption band at 691 nm. Similarly, the peaks at 346, 460 and 500 nm are seen to partially bleach to leave a single broad absorption at 440 nm. Importantly, there is no clear isobestic point in the spectra as they evolve, suggesting that the conversion involves multiple steps and species. Exposure of the sample generated in Figure 3.1b to air eventually regenerates the spectrum of the initial complex, \mathbf{P}_h^{4+} , however in this case, the regeneration process is very slow requiring approximately 12 h to complete.

The results of this photochemical experiment are qualitatively similar to those observed for irradiation of \mathbf{P}_c^{4+} under identical conditions. Irradiation of \mathbf{P}_c^{4+} leads to two sequential changes to the absorption spectrum which we know are associated with Equations 3.1 and 3.2, in which the electrons and proton ultimately come from the sacrificial donor, TEA.^{35, 75, 78}



The first reduction to form \mathbf{P}_c^{3+} results in the appearance of an intense peak at 965 nm with overtones at 855 nm. Upon undergoing the second reduction and protonation to form \mathbf{HP}_c^{3+} , the near-IR peak is bleached and a new structured peak at ~715 nm is observed.^{35, 76}

The similarity in the evolution of the absorption spectra of \mathbf{P}_h^{4+} and \mathbf{P}_c^{4+} in MeCN upon irradiation suggests similar photoreductive processes are occurring in both complexes.³⁵ With this evidence, we hypothesize that visible light excitation of the MLCT band in \mathbf{P}_h^{4+} leads to a photoexcited state which is reductively quenched by TEA to yield the monoreduced complex \mathbf{P}_h^{3+} , the absorption spectrum of which is shown in Figure 3.1a. We further hypothesize that absorption into the MLCT band of \mathbf{P}_h^{3+} leads to a photoexcited state which is reductively quenched by TEA to yield the doubly-reduced complex \mathbf{P}_h^{2+} , which may or may not be

protonated, and has the absorption spectrum shown in Figure 3.1b. Thus it appears that \mathbf{P}_h^{4+} , like \mathbf{P}_c^{4+} , is capable of photodriven multi-electron storage and significantly, these photoreduced forms of \mathbf{P}_h^{4+} , are more potently reducing!

3.3.2 Chemical Reduction of $[(phen)_2Ru(tatpp_h)Ru(phen)_2]^{4+}$

While the similarity in the evolution of the absorption spectra in MeCN of \mathbf{P}_h^{4+} and \mathbf{P}_c^{4+} upon irradiation is striking, this alone does not prove that the two photochemical processes are indeed analogous. In a separate set of experiments, stoichiometric reductions of \mathbf{P}_h^{4+} were performed in MeCN using cobaltocene ($Co(Cp)_2$) as a one-electron reducing agent (see Equations 3.3 and 3.4). Oxidation of the violet-colored $Co(Cp)_2$ to $Co(Cp)_2^+$ results in a colorless solution in the visible portion of the spectrum.



The results of the titrations of \mathbf{P}_h^{4+} with 1 and 2 equivalents of cobaltocene are shown in Figure 3.2. The absorption spectra obtained immediately after addition of 1 or 2 equivalents of cobaltocene are shown in Fig. 3.2a. As can be seen, these two spectra are nearly identical to the spectrum obtained from the first photochemical process shown in Figure 3.1a and show a pronounced new peak at 918 nm, as well as some structured peaks in the 400-500 nm region. The appearance of the band at 918 nm upon one-electron reduction confirmed our hypothesis that the first photochemical process was indeed reductive quenching of the photoexcited \mathbf{P}_h^{4+} to yield \mathbf{P}_h^{3+} . The evolution of two similar spectra upon addition of 1 or 2 equivalents of cobaltocene was not completely unexpected. The reduction potential of cobaltocene is -0.79 V vs. NHE whereas the redox potential for the $\mathbf{P}_h^{3+/2+}$ is -0.96 V vs. NHE, thus the reaction is close to being thermoneutral. However, if we let the solution react overnight, the spectrum evolves slowly to yield the spectrum seen in Figure 3.2b. In this case, the driving force for the reaction is the poor reversibility of the $Co(Cp)_2^{+/0}$ couple. The spectrum of \mathbf{P}_h^{2+} generated with cobaltocene

is nearly identical to the spectrum obtained after the second photochemical process seen in Figure 3.1b. These titrations reveal that the photochemistry of P_h^{4+} is very similar to that of P_c^{4+} ,

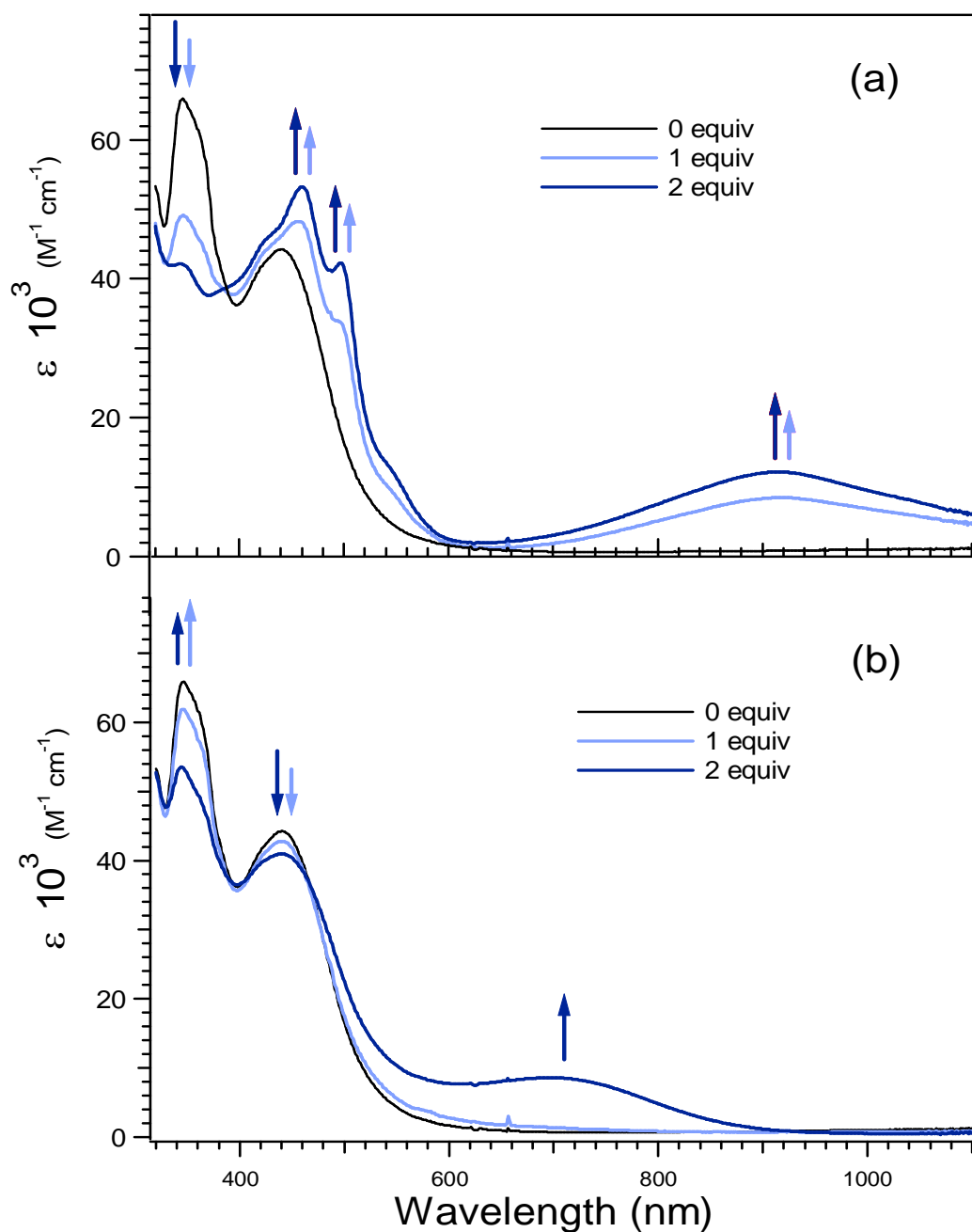


Figure 3.2 Evolution of the absorption spectra of P_h^{4+} upon chemical reduction by cobaltocene in MeCN ($16 \mu\text{M } P_h^{4+}$, 150 W tungsten bulb, 20°C)
 (a) immediately after addition of cobaltocene (b) overnight.

and that both complexes undergo two sequential one-electron photoreductions in the presence of appropriate sacrificial donors.

Interestingly, the spectrum of the mono-reduced complex P_h^{3+} was seen to bleach upon standing overnight, as seen in Figure 3.2b. This species formally has an unpaired electron trapped on the tatpp_h bridge and the reactivity of this radical may explain its instability upon prolonged standing. We attempted to stoichiometrically protonate the reduced complexes P_h^{3+} and P_h^{2+} by addition of controlled amounts of trifluoroacetic acid, however, the spectra obtained were of limited value and mostly appeared to be the initial complex P_h^{4+} .

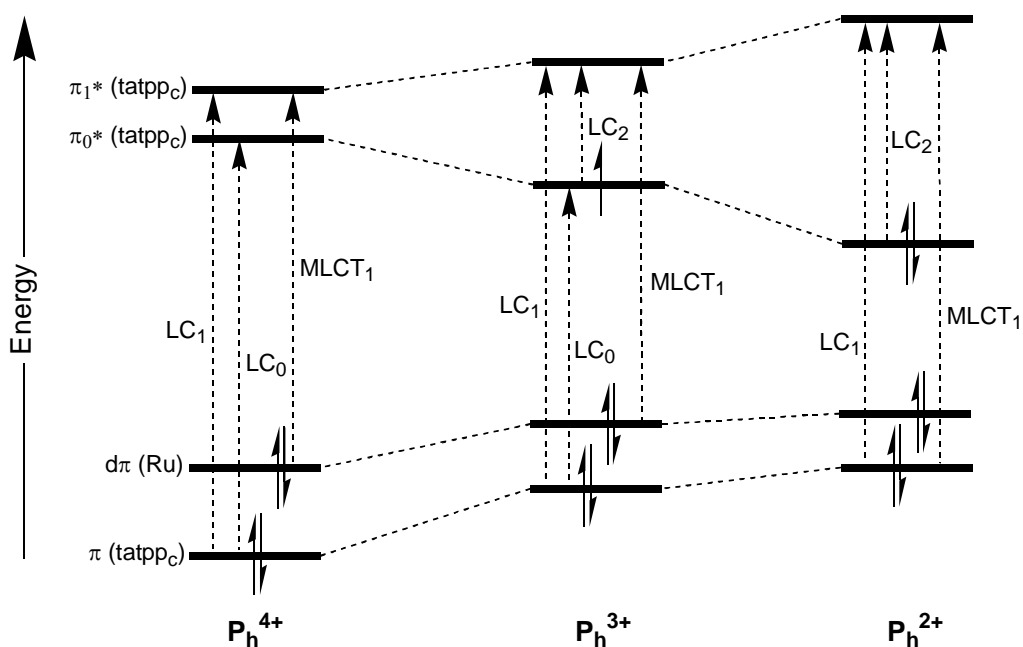


Figure 3.3 MO energy diagram of P_h^{4+} , P_h^{3+} , and P_h^{2+} .

The MO diagram shown in Figure 3.3 is based on our previous MO diagram seen in Figure 2.8, and is used to explain the observed changes in the optical spectrum upon reduction. The spectrum of P_h^{4+} is comprised of three major bands, LC_1 , LC_0 and $MLCT_1$, which are observed at 346, 440 and 441 nm respectively. The latter two bands are overlapped and not resolved. Upon reduction to P_h^{3+} , the π_0^* is now singly populated and is lowered in energy by

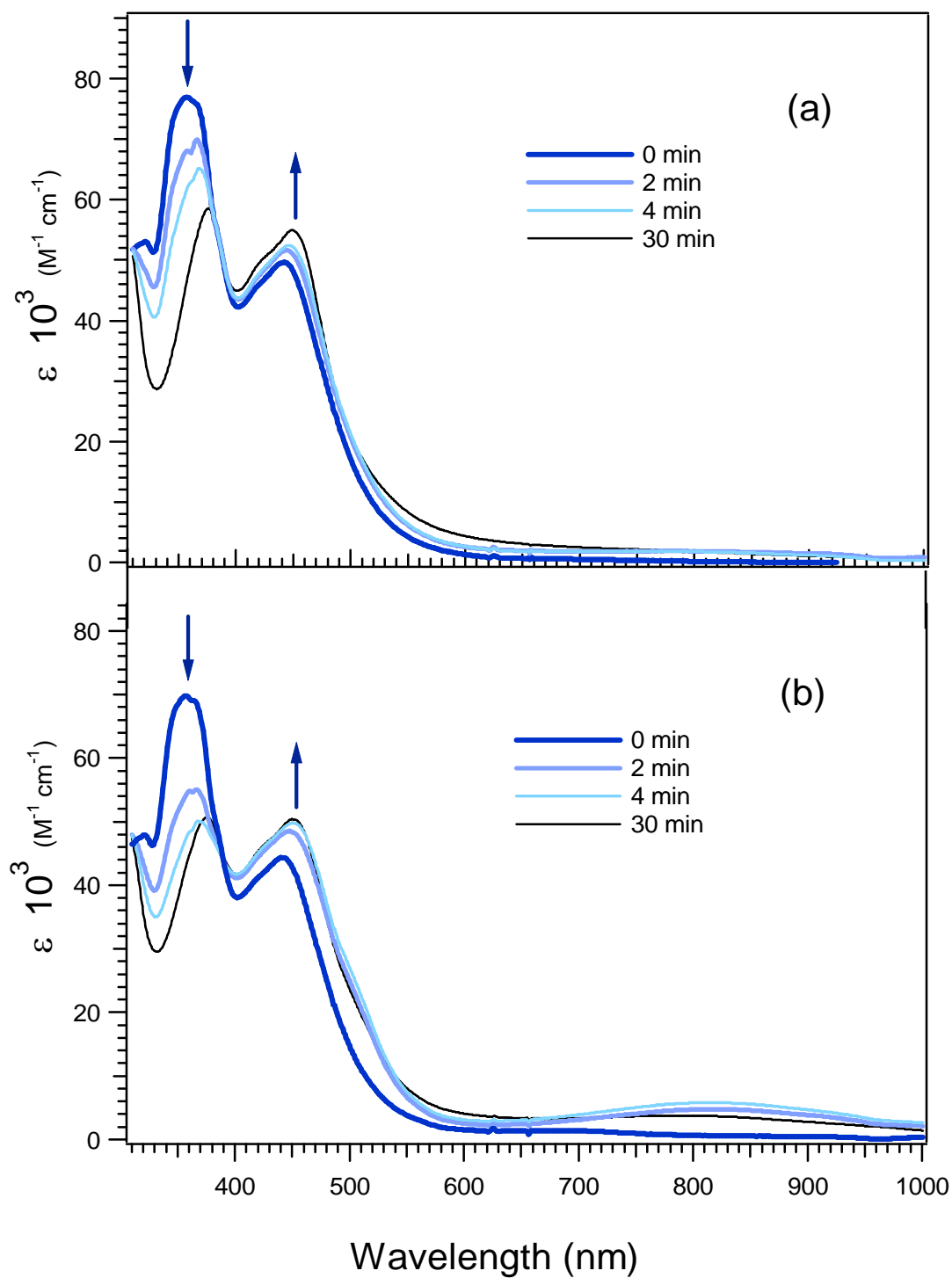


Figure 3.4 Evolution of the absorption spectra of P_n^{4+} during photoirradiation in water ($16 \mu\text{M } P_n^{4+}$, 0.25 M TEOA , $150 \text{ W tungsten bulb}$, $20 \text{ }^\circ\text{C}$) (a) pH 9 (b) pH 11.

bond reorganization to accommodate the new charge. A new low energy transition (LC_2) between π_0^* and π_1^* is now possible for the new complex and is seen at 918 nm. Addition of a second electron to the π_0^* orbital gives P_h^{2+} which fills this orbital and further stabilizes it due to bond reorganization. The resulting gap between the π_0^* and π_1^* increases and therefore the new LC_2 transition blue shifts to ~691 nm as is seen in Figure 3.2b. A qualitatively similar MO diagram was constructed to explain the absorption spectra of P_c^{4+} , P_c^{3+} , and P_c^{2+} .^{35, 75, 76}

3.3.3 Photoreduction of $[(phen)_2Ru(tatpp_h)Ru(phen)_2]^{4+}$ in Water

The photochemistry of P_h^{4+} in aqueous solution was also examined using triethanolamine (TEOA) as the sacrificial donor. Unlike P_c^{4+} which shows rich photochemistry in solutions down to pH 7, P_h^{4+} has been observed to undergo photoreduction only at highly basic conditions, e.g. pH~11 or greater. As can be seen in Figure 3.4a, minimal changes are seen in the absorption spectra of P_h^{4+} at pH 9, although there is a noticeable bleaching of the peak at 346 nm. At pH 11, the changes are more substantive, see Figure 3.4b, and upon prolonged irradiation the appearance of the broad absorption in the near IR peaking at 815 nm is observed.

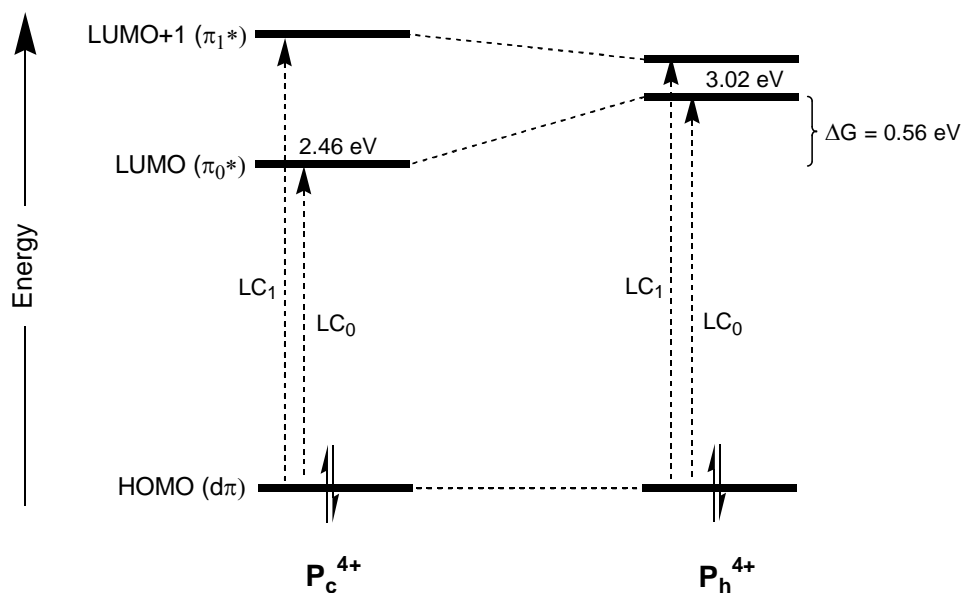


Figure 3.5 MO diagram of P_c^{4+} and P_h^{4+} and their approximate LUMO energies based on the DFT calculation.

3.4 Summary and Conclusion

A new complex, \mathbf{P}_h^{4+} , has been shown to absorb in the visible region at fairly strong intensity ($\epsilon = 40,000 \text{ M}^{-1}\text{cm}^{-1}$) through MLCT excitation. The confirmation of visible light excitation is important in our goal to prepare a photocatalyst that can harness visible light to produce hydrogen. This complex has also been found electrochemically to undergo two sequential reductions at more negative potentials than its linear analogue, \mathbf{P}_c^{4+} . These results correlate very well with the molecular orbital calculations. As shown in Figure 3.5, population of the \mathbf{P}_h^{4+} LUMO should result in a stored potential that is 0.56 eV (54 kJ/mol) higher than a similar population of the \mathbf{P}_c^{4+} LUMO.

Photochemically, \mathbf{P}_h^{4+} has been shown to undergo two sequential 1-electron photoreductions in MeCN generating singly (\mathbf{P}_h^{3+}) and doubly (\mathbf{P}_h^{2+}) reduced species that are thermodynamically capable of reducing H^+ to H_2 . In aqueous solvents however, the results are confusing and poorly behaved and somewhat disappointing. So far, the only indication of a photoreduction of \mathbf{P}_h^{4+} is at $\text{pH} \geq 11$. In contrast, the generation of the photoreduced forms of \mathbf{P}_c^{4+} at various degrees of protonation can be clearly observed through their characteristic spectra down to $\text{pH} 7$. As of this time, we are unable to draw any clear conclusions from our observations and may need further studies to gain a better understanding of the system's behavior in water. Further modifications of the structure of \mathbf{P}_h^{4+} , including the incorporation of a platinum co-catalyst into its structure as shown in Figure 3.6 is also being considered.

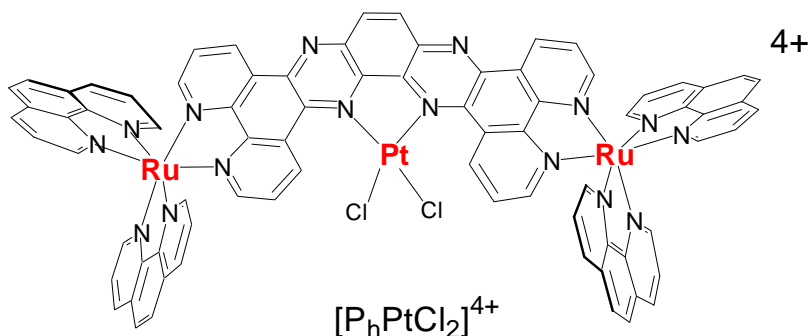
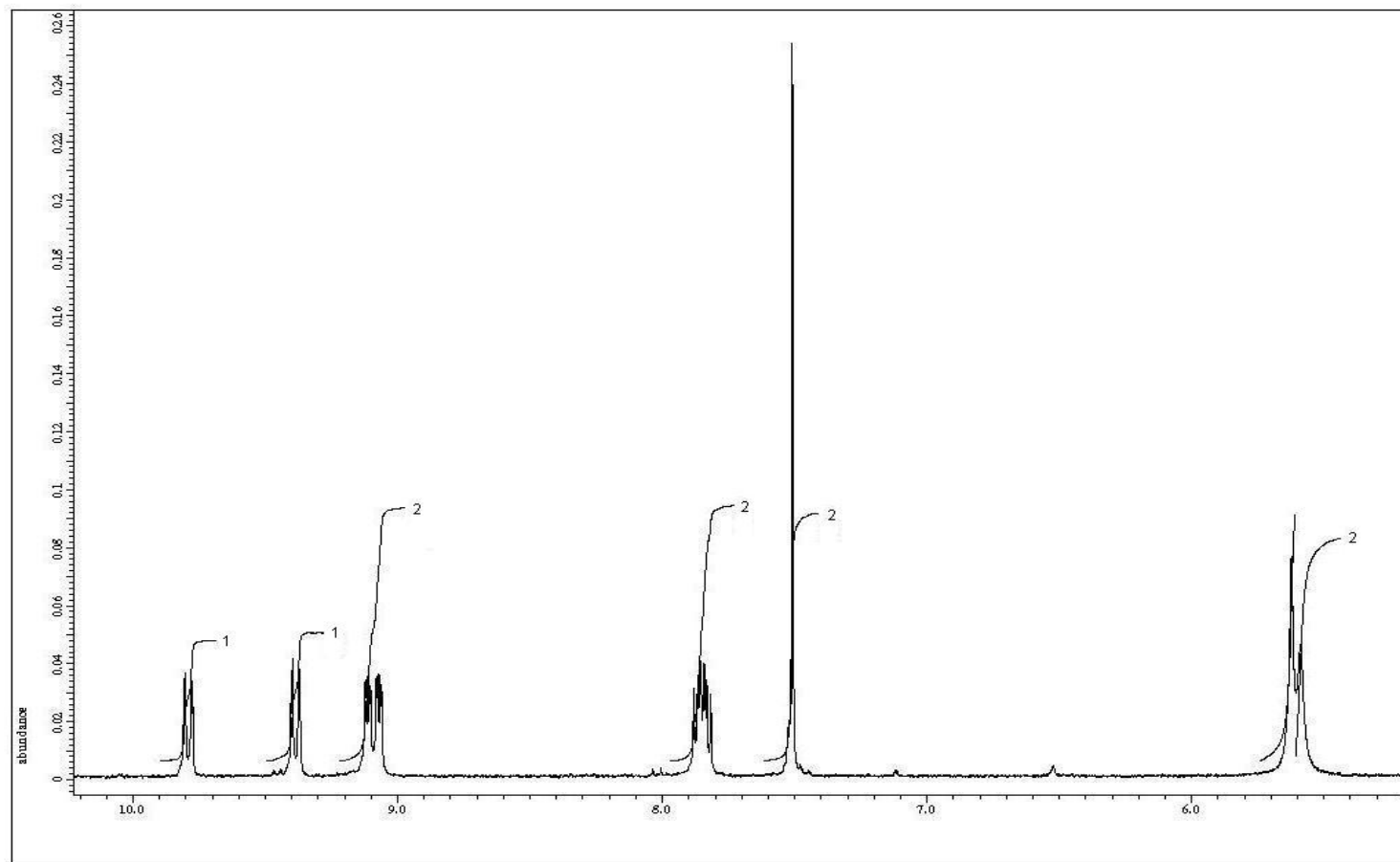


Figure 3.6. Structure of the planned complex, $[\mathbf{P}_h\text{PtCl}_2]^{4+}$.

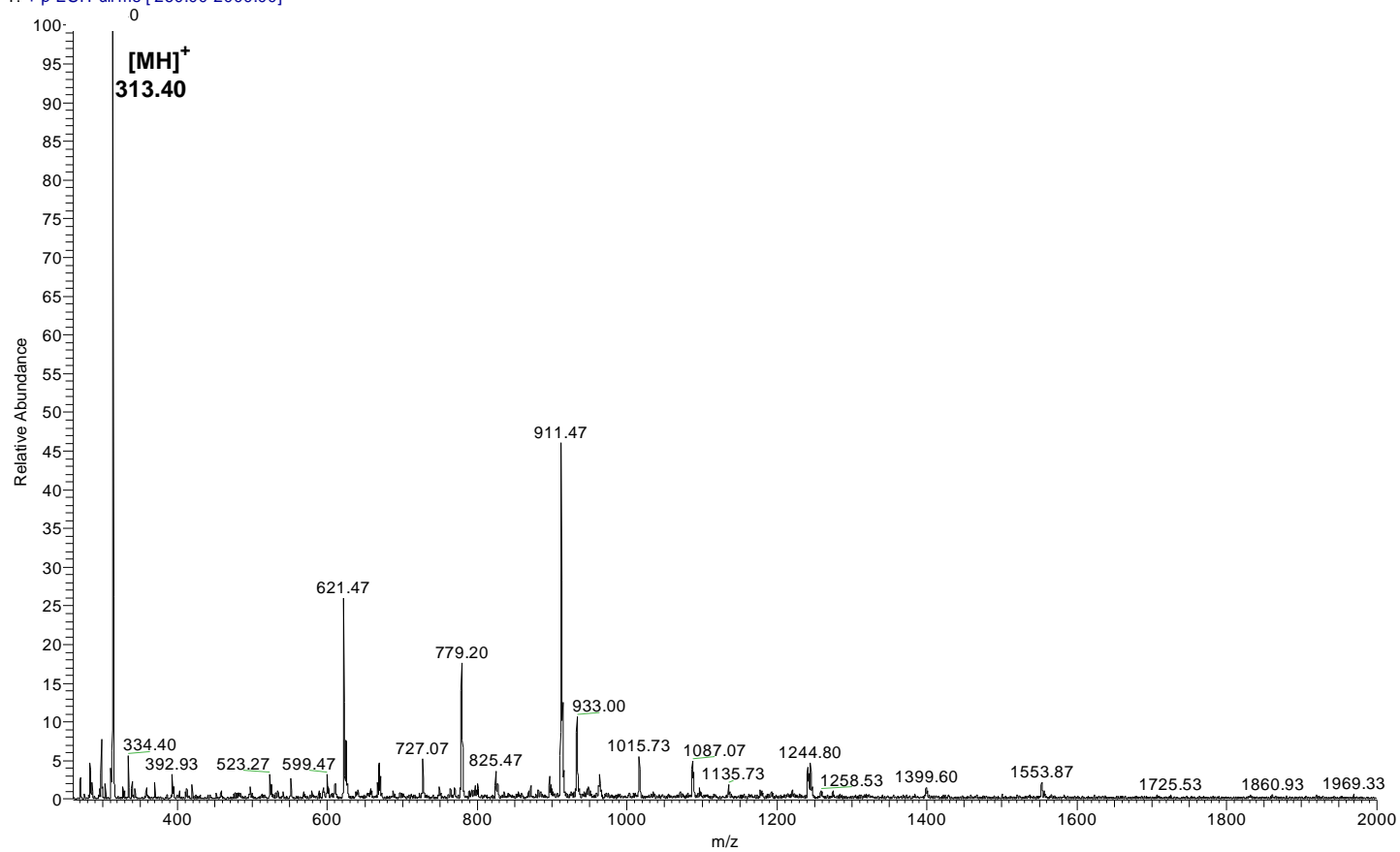
APPENDIX A

¹H NMR AND ESI-MS SPECTRA OF 10,11-diaminodppz



^1H NMR spectrum of 10,11-diaminodppz in DMSO-d_6

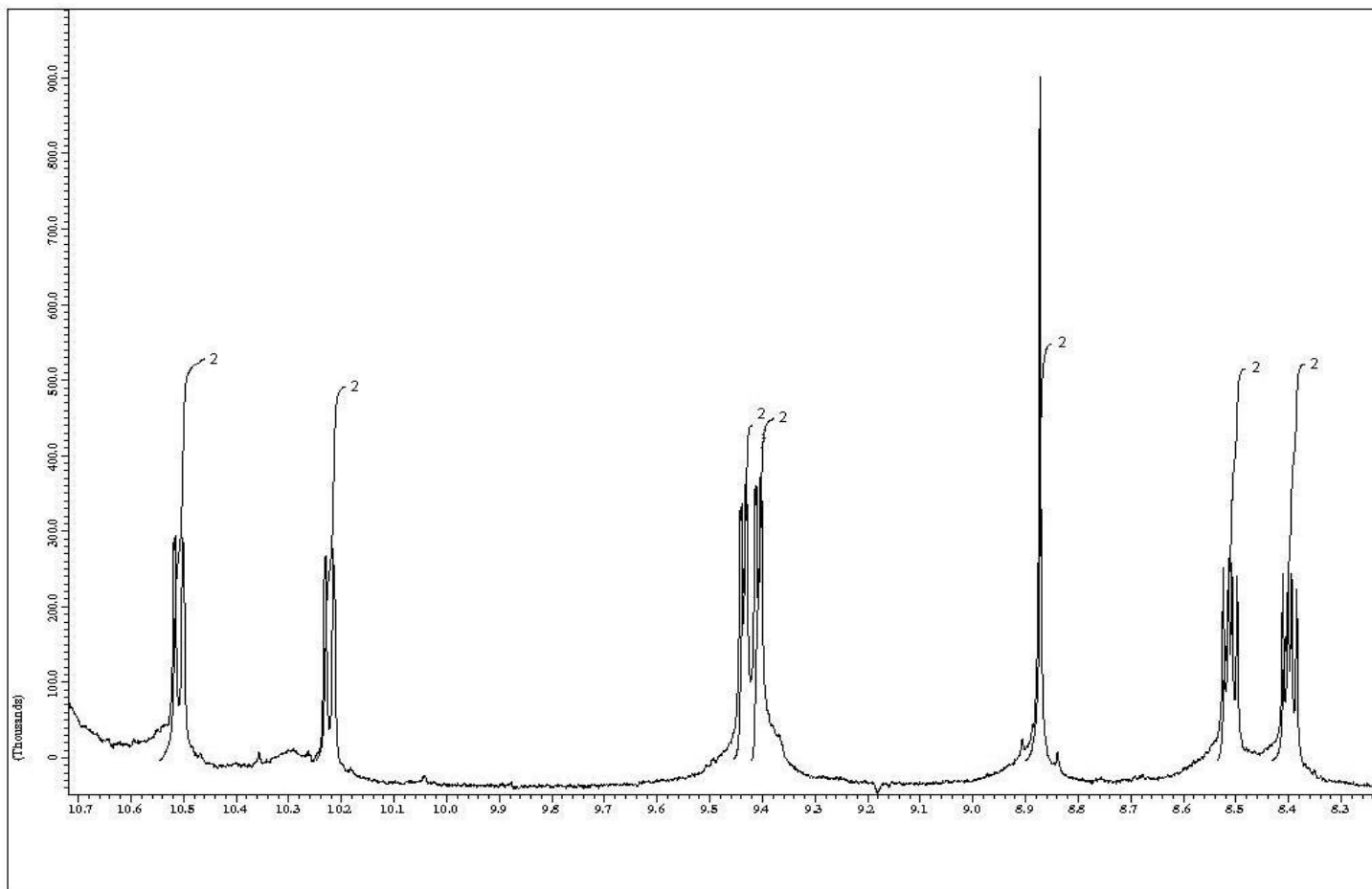
MSext459 #2-48 RT: 0.03-1.20 AV: 47 NL: 4.07E6
T: + p ESI Full ms [260.00-2000.00]



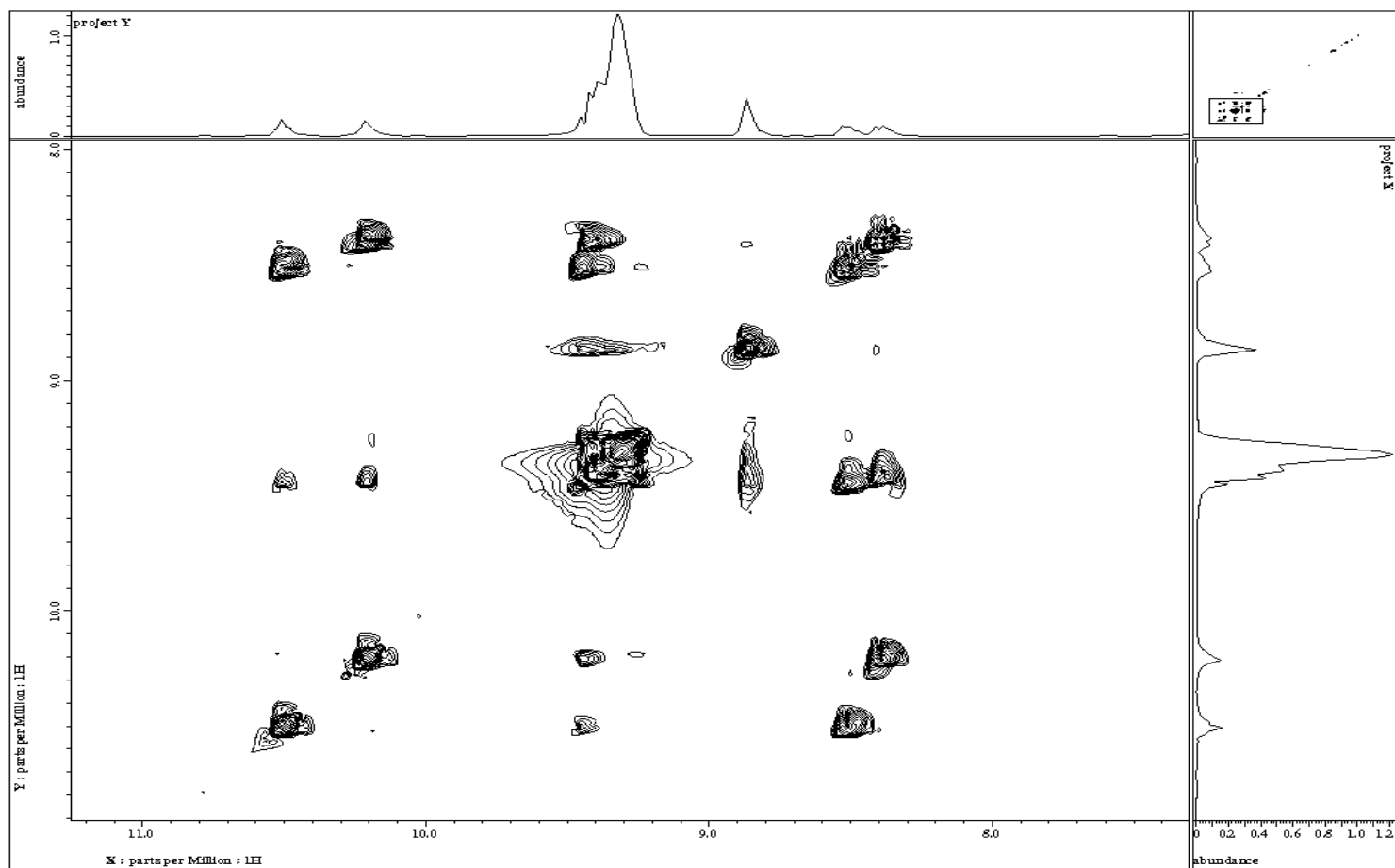
ESI-MS spectrum of 10,11-diaminodppz

APPENDIX B

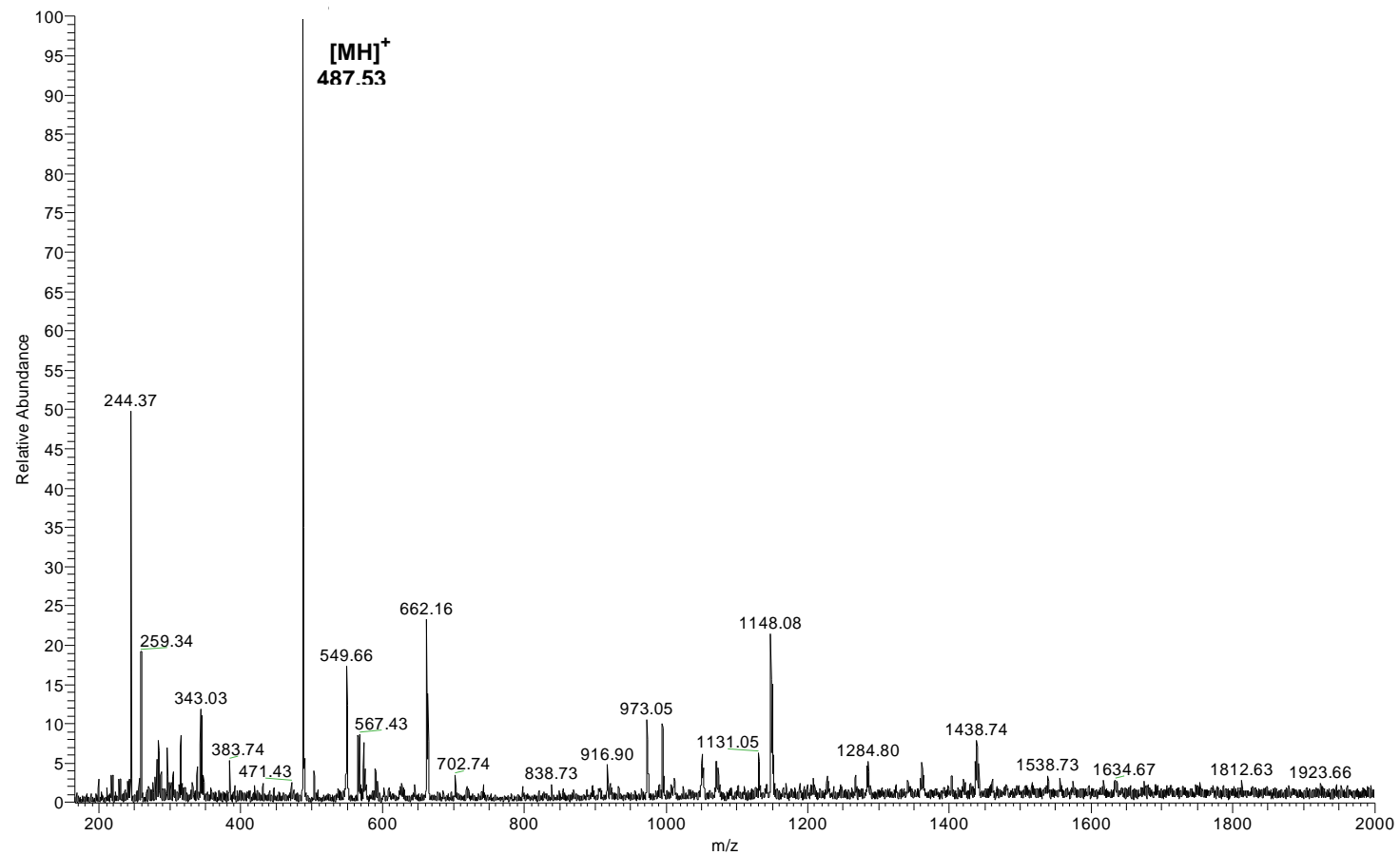
^1H NMR, COSY AND ESI-MS SPECTRA OF tatpp_n



^1H NMR spectrum of tatpp_h in CDCl_3 -TFA

COSY spectrum of tatpp_h in CDCl_3 -TFA

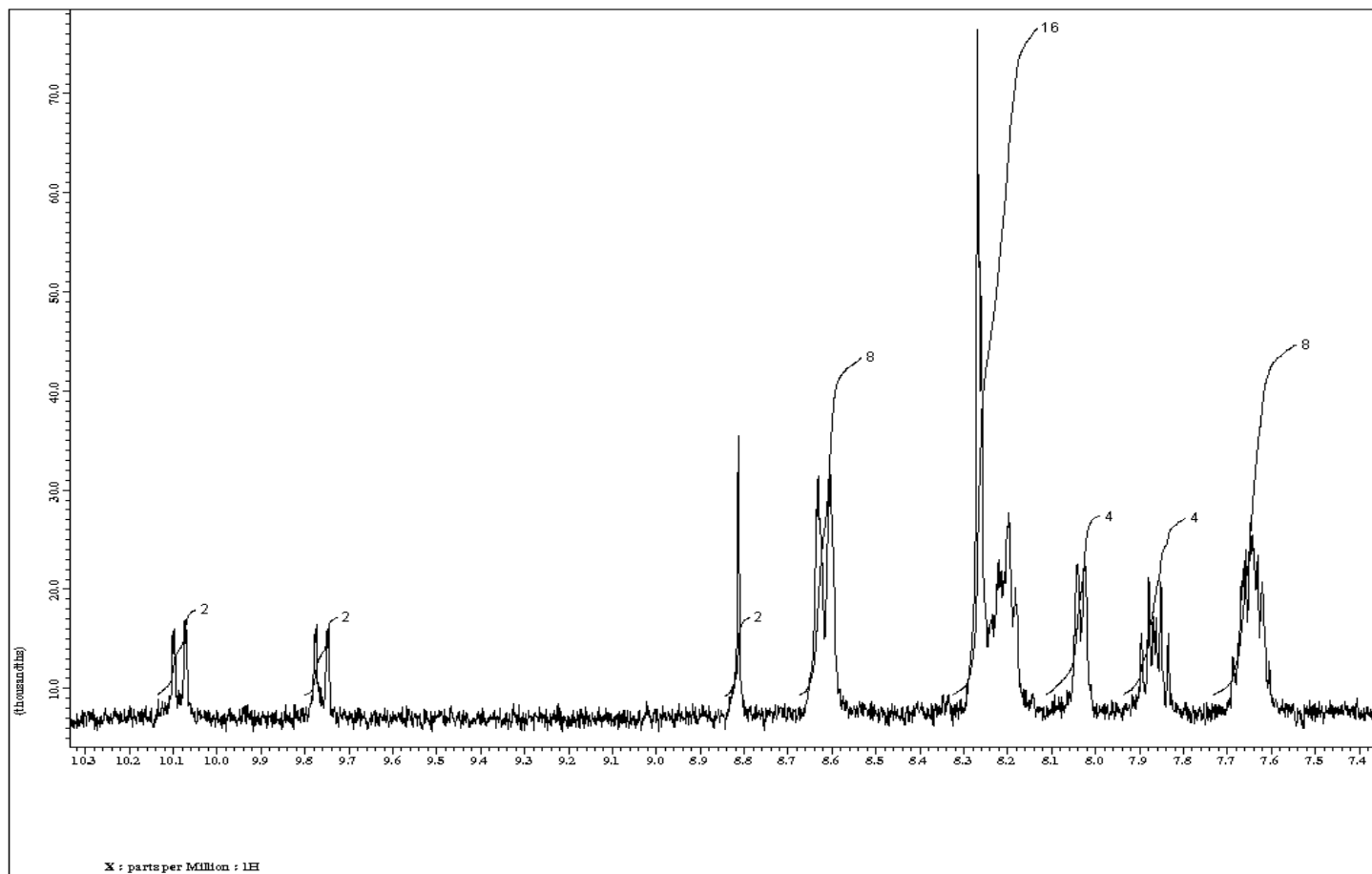
MSext647 #2-91 RT: 0.03-2.39 AV: 90 NL: 5.88E6
T: +p ESI Full ms [165.00-2000.00]



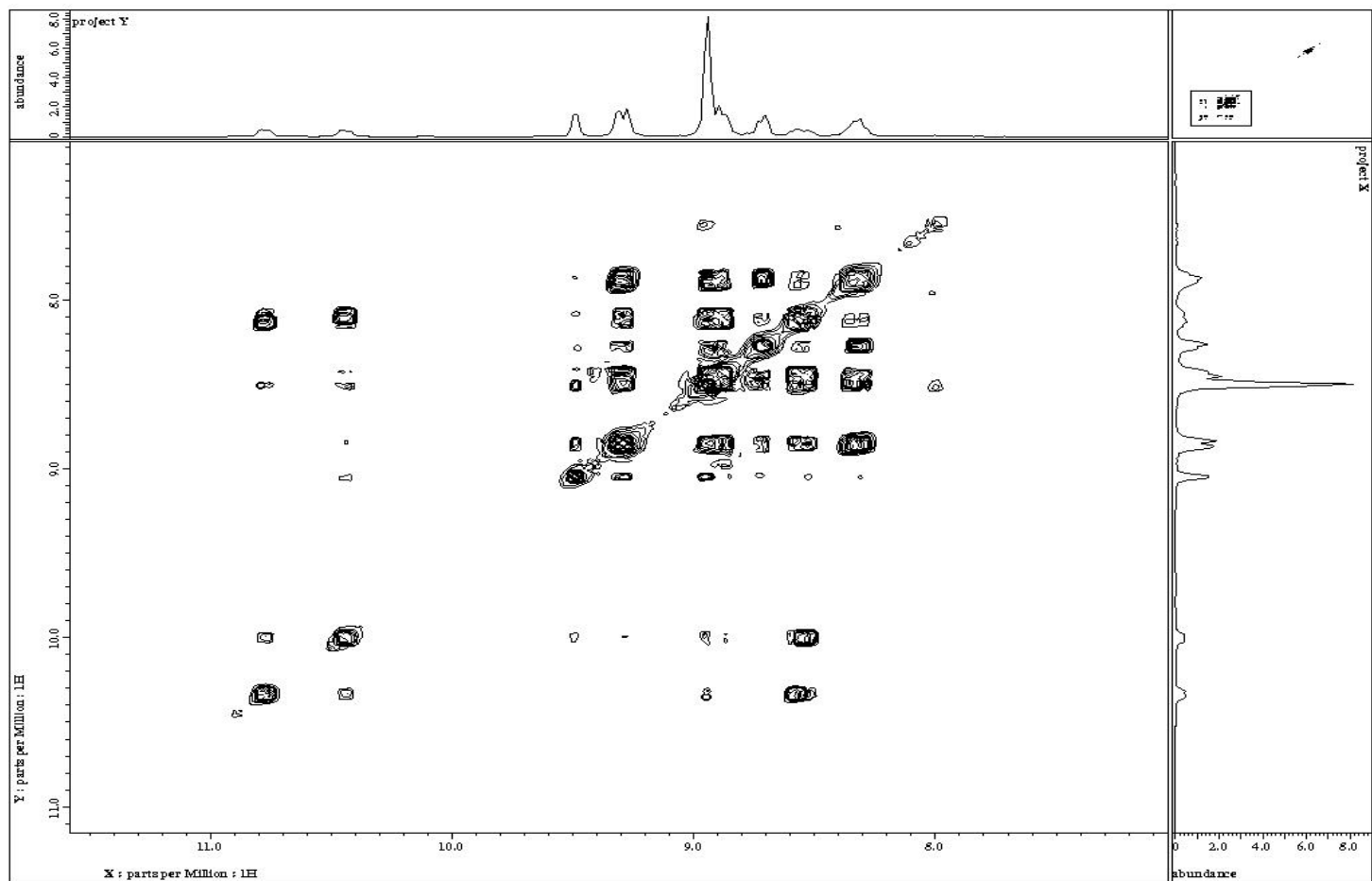
ESI-MS spectrum of tatpp_h

APPENDIX C

^1H NMR AND COSY SPECTRA of P_h^{4+}



^1H NMR spectrum of P_n^{4+} in MeCN



^1H NMR spectrum of P_n^{4+} in MeCN

REFERENCES

1. Aitken, D. W. *Transitioning to a Renewable Energy Future*; The International Solar Energy Society: 2003.
2. Meeting the International Clean Energy and Climate Change Challenges. http://www.whitehouse.gov/the_press_office/Fact-Sheet-Meeting-the-International-Clean-Energy-and-Climate-Change-Challenges/ (accessed July, 20, 2009).
3. *Renewables in Global Energy Supply*; International Energy Agency: Paris, January 2007.
4. *2007 Survey of Energy Resources*; World Energy Council: 2007.
5. Schlapbach, L.; Züttel, A., *Nature* **2001**, *414*, 353-358.
6. Salisbury, F. B.; Ross, C. W., *Plant Physiology*. 4th ed.; Wadsworth Publishing Company: Belmont, 1992.
7. Taiz, L.; Zeiger, E., *Plant Physiology*. fourth ed.; Sinauer Associates, Inc.: 2006; p 700.
8. Hopkins, W. G.; Huner, N. P. A., *Introduction to Plant Physiology*. 3rd ed.; John Wiley & Sons, Inc.: 2004.
9. Abrahamsson, M. L. A. Electron Transfer in Ruthenium-Manganese Complexes for Artificial Photosynthesis. Dissertation, Uppsala University, Uppsala, 2001.
10. Goldsmith, J. I.; Hudson, W. R.; Lowry, M. S.; Anderson, T. H.; Bernhard, S., *J. Am. Chem. Soc.* **2005**, *127* (20), 7502-7510.
11. Balzani, V.; Credi, A.; Venturi, M., *Chem. Eur. J.* **2002**, *8* (24), 5524-5532.
12. Sykora, M.; Maxwell, K. A.; DeSimone, J. M.; Meyer, T. J., *Proc. Nat. Acad. Sci. USA* **2000**, *97* (14), 7687-7691.
13. Cristian, L.; Piotrowiak, P.; Farid, R. S., *J. Am. Chem. Soc.* **2003**, *125*, 11814-11815.

14. Alstrum-Acevedo, J. H.; Brennaman, M. K.; Meyer, T. J., *Inorg. Chem.* **2005**, *44* (20), 6802-6827.
15. Fujihara, K.; Ohno, T.; Matsumura, M., *Faraday Trans.* **1998**, *94* (24), 3705-3709.
16. Fujishima, A.; Honda, K., *Nature* **1972**, *238* (5358), 37-8.
17. Khaselev, O.; Turner, J. A., *Science* **1998**, *280* (5362), 425-427.
18. Gratzel, M., *Nature* **2001**, *414*, 338.
19. Kim, M.-J.; Konduri, R.; Ye, H.; MacDonnell, F. M.; Puntoriero, F.; Serroni, S.; Campagna, S.; Holder, T.; Kinsel, G.; Rajeshwar, R., *Inorg. Chem.* **2002**, *41* (9), 2471-2476.
20. Elvington, M.; Brown, J.; Arachchige, S. M.; Brewer, K. J., *J. Am. Chem. Soc.* **2007**, *129* (35), 10644-10645.
21. Rau, S.; Schafer, B.; Gleich, D.; Anders, E.; Friedrich, M.; Górls, H.; Henry, W.; Vos, J. G., *Angew. Chem. Intern. Ed.* **2006**, *45*, 6215-6218.
22. Ozawa; Haga, M.-A.; Sakai, K., *J. Am. Chem. Soc.* **2006**, *128*, 4926-4927.
23. Wasielewski, M. R.; Niemczyk, M. P.; Svec, W. A.; Pewitt, E. B., *J. Am. Chem. Soc.* **1985**, *107*, 5562-5563.
24. Molnar, S. M.; Nallas, G.; Bridgewater, J. S.; Brewer, K. J., *J. Am. Chem. Soc.* **1994**, *116*, 5206-5210.
25. MacDonnell, F. M., Molecular Approaches to Photochemical Splitting of Water. In *Solar Hydrogen Generation: Toward a Renewable Energy Future.*, Rajeshwar, K.; McConnell, R.; Licht, S., Eds. Springer Publishers: New York, 2008.
26. Serway, R.; Beichner, R., *Physics for Scientists and Engineers with Modern Physics*. 5th ed.; Saunders College Publishing: Orlando, 2000.
27. Sutin, N.; Creutz, C., Light induced electron transfer reactions of metal complexes. In *VIIIth International Union of Pure and Applied Chemistry symposium on photochemistry.*, Seefeld, Austria, 1980.

28. McEvoy, J. P.; Gascon, J. A.; Batista, V. S.; Brudvig, G. W., *Photochem. Photobiol. Sci.* **2005**, *4*, 940-949.
29. Balzani, V.; De Cola, L.; Prodi, L.; Scandola, F., *Pure & Appl. Chem.* **1990**, *62* (8), 1457-1466.
30. Krishtalik, L. I., *Biochim. Biophys. Acta* **1986**, *849*.
31. Gilbert, J. A.; Eggleston, D. S.; Murphy, W. R.; Geselowitz, D. A.; Gersten, S. W.; Hodgson, D. J.; Meyer, T. J., *J. Am. Chem. Soc.* **1985**, *107*, 3855-3864.
32. Binstead, R. A.; Chronister, C. W.; Ni, J.; Hartshorn, C. M.; Meyer, T. J., *J. Am. Chem. Soc.* **2000**, *122*, 8464-8473.
33. Sartorel, A.; Carraro, M.; Scorrano, G.; De Zorzi, R.; Geremia, S.; McDaniel, N. D.; Bernhard, S.; Bonchio, M., *J. Am. Chem. Soc.* **2008**, *130*, 5006-5007.
34. Konduri, R.; Ye, H.; MacDonnell, F. M.; Serroni, S.; Campagna, S.; Rajeshwar, K., *Angew. Chem. Int. Ed.* **2002**, *41* (17), 3185-3187.
35. Wouters, K. L.; de Tacconi, N. R.; Konduri, R.; Lezna, R. O.; MacDonnell, F. M., *Photosynth. Res.* **2006**, *87*, 41-55.
36. Elvington, M.; Brewer, K. J., *Inorg. Chem.* **2006**, *45* (14), 5242-5244.
37. Kiwi, J.; Gratzel, M., *Nature* **1979**, *281*, 657-658.
38. Kalyanasundaram, K., *Photochemistry of Polypyridine and Porphyrin Complexes*. Academic Press: London, 1992.
39. Tinker, L. L. M., N. D.; Curtin, P. N.; Smith, C. K.; Ireland, M. J.; Bernhard, S., *Chem. Eur. J.* **2007**, *13*, 8726-8732.
40. Crosby, G. A., *Acc. Chem. Res.* **1975**, *8*, 231-238.
41. Balzani, V.; Juris, A.; Venturi, M.; Campagna, S.; Serroni, S., *Chem. Rev.* **1996**, *96*, 759-833.
42. Meyer, T. J., *Pure & Appl. Chem.* **1986**, *58* (9), 1193-1206.

43. Turro, N. J., *Modern Molecular Photochemistry*. University Science Books: Sausalito, 1991.
44. Abrahamsson, M. Tuning of the Excited State Properties of Ruthenium(II)-Polypyridyl Complexes. Dissertation, Uppsala University, Uppsala, 2006.
45. Sauvage, J., -P.; Collin, J., -P.; Chambron, J.-C.; Guillerez, S.; Coudret, C., *Chem. Rev.* **1994**, *94* (4), 993-1019.
46. *Marcus equation*; BNL--65855; Other: ON: DE99000575; BR: KC030101; 1998.
47. Housecroft, C. E.; Sharpe, A. G., *Inorganic Chemistry*. 2nd ed.; Pearson Education Ltd.: 2005.
48. Shriver, D. F.; Atkins, P. W., *Inorganic Chemistry*. 3rd ed.; W. H. Freeman and Co: New York, NY, 1999.
49. Marcus, R. A.; Sutin, N. In *Application of Electron-Transfer Theory to Several Systems of Biological Interest*, Workshop on Antennas and Reaction Centers of Photosynthetic Bacteria - Structure, Interactions and Dynamics., Feldafing, West Germany, Feldafing, West Germany, 1985.
50. Creutz, C.; Sutin, N., *Proc. Nat. Acad. Sci. USA* **1975**, *72* (8), 2858-2862.
51. Sutin, N., *J. Photochem.* **1979**, *10*, 19-40.
52. Gafney, H. D.; Adamson, A. W., *J. Am. Chem. Soc.* **1972**, *94*, 8238-8239.
53. McAlister, C. Coupling Photodriven Multielectron Reduction Of Ruthenium Polypyridyl Complexes With Hydrogen Evolving Co-catalysts. M.S. Thesis, University of Texas at Arlington, Arlington, 2007.
54. Paw, W.; Eisenberg, R., *Inorg. Chem.* **1997**, *36* (11), 2287-2293.
55. Nakabayashi, Y.; Watanabe, Y.; Nakao, T.; Yamauchi, O., *Inorg. Chim. Acta* **2004**, *357*, 2553–2560.
56. Amouyal, E.; Homsy, A.; Chambron, J.-C.; Sauvage, J.-P., *Dalton Trans.* **1990**, 1841-1845.

57. Mattay, J.; Kleineweischede, A., *A. Eur. J. Org. Chem.* **2006**, 947-957.
58. Pietra, S.; Casiraghi, G., *Gazz. Chim. Ital.* **1967**, 97, 1826-1836.
59. Vogel, A. I., *Vogel's Textbook of Practical Organic Chemistry*. 4th ed.; Longman: London, 1978.
60. Jolly, W. L.; Becke-Goehring, M., *Inorg. Chem.* **1962**, 1 (1), 76-78.
61. Mataka, S.; Ikezaki, Y.; Takahashi, K.; Tori-i, A.; Tashiro, M., *Heterocycles* **1992**, 33 (2), 791-800.
62. Bodige, S.; Torres, A. S.; Maloney, D. J.; Tate, D.; Kinsel, G. R.; Walker, A. K.; MacDonnell, F. M., *J. Am. Chem. Soc.* **1997**, 119 (43), 10364.
63. Campagna, S.; Serroni, S.; Bodige, S.; MacDonnell, F. M., *Inorg. Chem.* **1999**, 38 (4), 692.
64. MacDonnell, F. M.; Bodige, S., *Inorg. Chem.* **1996**, 35 (20), 5758.
65. Kim, M.-J.; MacDonnell, F. M.; Gimon-Kinsel, M. E.; Du Bois, T.; Asgharian, N.; Griener, J. C., *Angew. Chem. Int. Ed.* **2000**, 39 (3), 615-619.
66. MacDonnell, F. M.; Ali, M. M.; Kim, M.-J., *Comments Inorg. Chem.* **2000**, 22 (3), 203-225.
67. Calvert, J. G.; Pitts, J. N., *Photochemistry*. John Wiley & Sons, Inc.: 1966.
68. Bolger, J.; Gourdon, A.; Ishow, E.; Launay, J.-P., *Inorg. Chem.* **1996**, 35 (10), 2937.
69. Ishow, E.; Gourdon, A.; Launay, J.-P.; Lecante, P.; Verelst, M.; Chiorboli, C.; Scandola, F.; Bignozzi, C.-A., *Inorg. Chem.* **1998**, 37 (14), 3603.
70. Ishow, E.; Gourdon, A.; Launay, J.-P.; Chiorboli, C.; Scandola, F., *Inorg. Chem.* **1999**, 38 (7), 1504.
71. Chiorboli, C.; Bignozzi, C. A.; Scandola, F.; Ishow, E.; Gourdon, A.; Launay, J.-P., *Inorg. Chem.* **1999**, 38 (10), 2402.
72. Flamigni, L.; Encinas, S.; Barigelletti, F.; MacDonnell, F. M.; Kim, K.-J.; Puntoriero, F.; Campagna, S., *Chem. Commun.* **2000**, (13), 1185-1186.

73. Chambron, J.-C.; Sauvage, J., -P.; Amouyal, E.; Kiffi, P., *Nouv. J. Chim.* **1985**, *9*.
74. Pletcher, D.; Greef, R.; Peat, R.; Peter, L. M.; Robinson, J., *Instrumental Methods in Electrochemistry*. Horwood Publishing: Chichester, 2001.
75. Konduri, R.; De Tacconi, N. R.; Rajeshwar, K.; MacDonnell, F. M., *J. Am. Chem. Soc.* **2004**, *126*, 11621-11629.
76. de Tacconi, N. R.; Lezna, R. O.; Konduri, R.; Ongeri, F.; Rajeshwar, K.; MacDonnell, F. M., *Chem. Eur. J.* **2005**, *11*, 4327-4339.
77. Parry, E. P.; Osteryoung, R. A., *Anal. Chem.* **1965**, *37*, 1634.
78. DeLaive, P. J.; Foreman, T. K.; Giannotti, C.; Whitten, D. G., *J. Am. Chem. Soc.* **1980**, *102* (17), 5627-5631.

BIOGRAPHICAL INFORMATION

Nancy Ruth G. Diaz was born and raised in the southern province of Zamboanga del Sur in the Philippines. She obtained her undergraduate degrees in Chemistry and Math from Far Eastern University in the year 1990. She worked for several years in the Philippines before immigrating to Canada in 2002. Pursued graduate studies in Chemistry at the University of Texas at Arlington in the spring of 2005. She obtained her M.S. degree in the summer of 2009 under the guidance of Prof. Frederick M. MacDonnell.